HHS Public Access

Author manuscript

Cell Rep. Author manuscript; available in PMC 2024 February 05.

Published in final edited form as:

Cell Rep. 2023 October 31; 42(10): 113171. doi:10.1016/j.celrep.2023.113171.

Myeloid *BAF60a* deficiency alters metabolic homeostasis and exacerbates atherosclerosis

Yang Zhao[1,2,6], **Yuhao Liu**[1,6], **Guizhen Zhao**[1], **Haocheng Lu**[1,3], **Yaozhong Liu**[1], **Chao Xue**[1], **Ziyi Chang**[1], **Hongyu Liu**[1], **Yongjie Deng**[1], **Wenying Liang**[1], **Huilun Wang**[1], **Oren Rom**[1,4], **Minerva T. Garcia-Barrio**[1], **Tianqing Zhu**[1], **Yanhong Guo**[1], **Lin Chang**[1], **Jiandie Lin**[5], **Y. Eugene Chen**[1,2], **Jifeng Zhang**[1,7,*]

[1]Department of Internal Medicine, Cardiovascular Center, University of Michigan Medical Center, Ann Arbor, MI 48109, USA

[2]Department of Pharmacology, University of Michigan Medical School, Ann Arbor, MI 48109, USA

[3]Department of Pharmacology, Southern University of Science and Technology, Shenzhen, Guangdong 518055, China

[4]Department of Pathology and Translational Pathobiology, Department of Molecular and Cellular Physiology, Louisiana State University Health Sciences Center – Shreveport, Shreveport, LA 71103, USA

[5]Life Sciences Institute and Department of Cell & Developmental Biology, University of Michigan Medical Center, Ann Arbor, MI 48109, USA

[6]These authors contributed equally

[7]Lead contact

SUMMARY

Atherosclerosis, a leading health concern, stems from the dynamic involvement of immune cells in vascular plaques. Despite its significance, the interplay between chromatin remodeling and transcriptional regulation in plaque macrophages is understudied. We discovered the reduced expression of *Baf60a*, a component of the switch/sucrose non-fermentable (SWI/SNF) chromatin remodeling complex, in macrophages from advanced plaques. Myeloid-specific *Baf60a* deletion compromised mitochondrial integrity and heightened adhesion, apoptosis, and plaque

*Correspondence: jifengz@umich.edu.

AUTHOR CONTRIBUTIONS

Y.Z., Yuhao Liu, G.Z., H.L., Z.C., and J.Z. performed experiments and analyzed the results. Y.Z. and J.Z. prepared the manuscript. Yaozhong Liu, C.X., W.L., H.W., H.L. Y.D., O.R., M.T.G.-B., T.Z., Y.G., L.C., and J.L. provided experimental and technical support. Y.E.C., M.T.G.-B., and J.Z. edited the manuscript. Y.Z., Yuhao Liu, and J.Z. contributed to the experimental design.

DECLARATION OF INTERESTS

The authors declare no competing interests.

DECLARATION OF GENERATIVE AI AND AI-ASSISTED TECHNOLOGIES IN THE WRITING PROCESS

During the preparation of this work the authors used ChatGPT from OpenAI for proofreading. After using this tool, the authors reviewed and edited the content as needed and take full responsibility for the content of the publication.

SUPPLEMENTAL INFORMATION

Supplemental information can be found online at https://doi.org/10.1016/j.celrep.2023.113171.

development. BAF60a preserves mitochondrial energy homeostasis under pro-atherogenic stimuli by retaining nuclear respiratory factor 1 (NRF1) accessibility at critical genes. Overexpression of *BAF60a* rescued mitochondrial dysfunction in an NRF1-dependent manner. This study illuminates the BAF60a-NRF1 axis as a mitochondrial function modulator in atherosclerosis, proposing the rejuvenation of perturbed chromatin remodeling machinery as a potential therapeutic target.

In brief

Yang et al. uncover the critical role of BAF60a, a subunit of the SWI/SNF chromatin remodeling complex, in maintaining macrophage mitochondrial homeostasis during atherogenesis. Their findings reveal a dysregulated chromatin remodeling-metabolic crosstalk and propose a potential approach for treating atherosclerosis by restoring impaired BAF60a-NRF1 communication.

Graphical Abstract

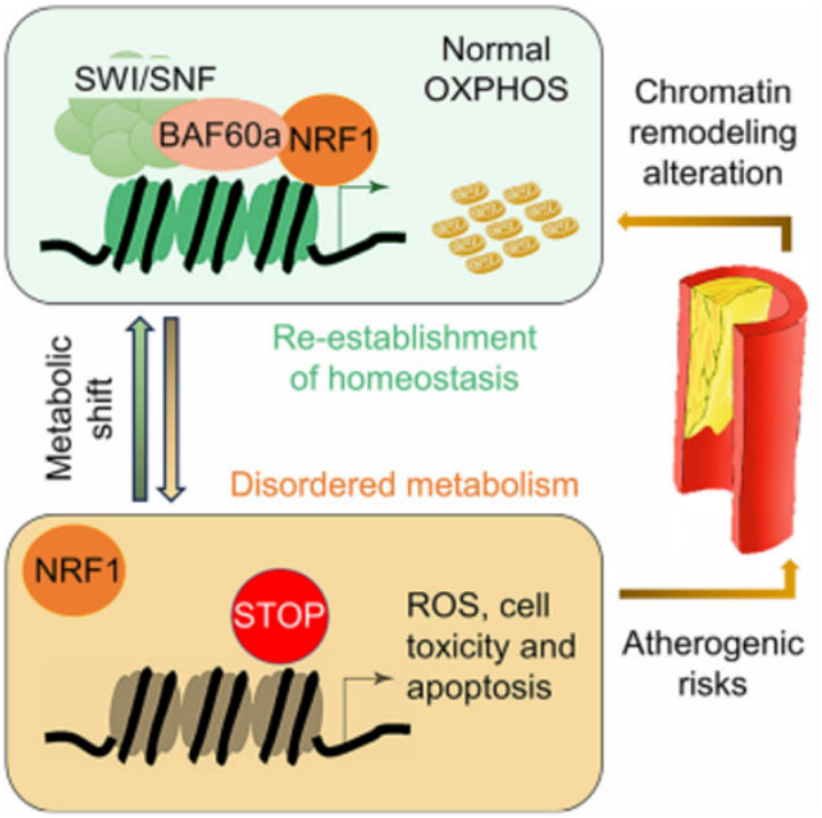

INTRODUCTION

Atherosclerosis is a complex pathological process characterized by the accumulation of plaques within arterial walls, resulting in inflammation, calcification, and potential plaque rupture. As the underpinning pathology of many cardiovascular diseases (CVDs), atherosclerosis is a primary health concern worldwide. Serious clinical manifestations of this pathology include myocardial infarction and stroke.[1,2] Despite advances in therapeutic strategies, notably low-density lipoprotein (LDL)-lowering agents such as statins and

PCSK9 inhibitors, residual cardiovascular risk remains a significant challenge.[3,4] Further, the utility of anti-inflammatory therapies in atherosclerosis has been predominantly confined to individuals with elevated systemic inflammatory markers, underscoring the need for alternative therapeutic avenues.[5,6]

Epigenetics, which encompasses changes in gene expression without underlying DNA sequence alterations, plays roles in various diseases, including CVDs. While genetic studies have unveiled variants associated with CVD risk, emerging evidence implicates epigenetic modifications—such as DNA methylation, histone modification, and ATP-dependent chromatin remodeling—as critical regulators of atherosclerosis.[7–14] These epigenetic shifts are often modulated by the disease microenvironment, impacting diverse cells, notably immune cells residing within the atherosclerotic plaques.

Among the implicated immune cells, macrophages are of paramount importance. These cells are not merely bystanders in atherosclerosis; they actively participate in all facets of plaque development, from initiation to progression and regression.[15–21] Their multifaceted roles encompass lipid uptake, secretion of inflammatory mediators, and modulation of the local cellular environment within plaques.[22]

Interestingly, macrophage functionality and phenotype are closely tied to metabolic and epigenetic modifications.[23,24] Environmental cues can elicit distinct metabolic and epigenetic reprogramming within macrophages, emphasizing the importance of understanding the interplay between these processes in atherosclerosis.[24–29]

The mammalian switch/sucrose non-fermentable (SWI/SNF) chromatin remodeling complex plays a pivotal role in modifying the chromatin landscape and thereby regulating gene expression.[30–32] Of note, we and others have reported that the three mutually exclusive and often adaptive BAF60a, BAF60b, and BAF60c subunits bridge the interaction between tissue-specific transcription factors (TFs)/co-factors and the SWI/SNF core complex to regulate gene-expression changes in response to various complications.[10,11,32–36] Our focus on BAF60a, in particular, stems from its emerging significance in various disease contexts and preliminary findings hinting at its pivotal role in macrophage functions. To date, the interaction of macrophage BAF60a with specific TFs within the atherosclerotic milieu has remained largely uncharted.

In the present study, we aimed to elucidate this intricate interaction. We delineate the consequences of *Baf60a* deficiency in macrophages, particularly its impact on mitochondrial function and atherosclerotic plaque development. By shedding light on the epigenetic-metabolic crosstalk in macrophages within the atherosclerotic environment, our findings unveil potential innovative avenues for therapeutic intervention.

RESULTS

Downregulation of *Baf60a* in advanced atherosclerotic plaque macrophages exacerbates atherosclerosis in *ApoE*$^{-/-}$ hypercholesterolemic mice

To explore the potential shifts in *Baf60a* expression in plaque macrophages, aortic cells from *ApoE*$^{-/-}$ mice fed a Western diet (WD, Figure 1A) were isolated using fluorescence-activated cell sorting (FACS). We identified a significant reduction in *Baf60a* expression in CD45/Galectin-3 (Mac2) double-positive macrophages at 16 weeks relative to 8 weeks ($p = 0.0005$). The decrease was exclusive to *Baf60a*, as *Baf60b* and *Baf60c* levels remained stable. Also importantly, this reduction was specific to macrophages in advanced atherosclerosis, as *Baf60a* expression in mixed aortic cells and pan-leukocyte populations remained unchanged (Figure 1B).

To emulate this downregulation and study its impact on atherosclerosis, we developed *Baf60a*^{mKO}/*ApoE*$^{-/-}$ mice and used *Baf60a*$^{f/f}$/*ApoE*$^{-/-}$ mice as littermate controls. Upon confirming the *Baf60a* deletion in bone marrow-derived macrophages (BMDMs), we detected no changes in other SWI/SNF complex components (Figures 1C, 1D, and S1A). After 16 weeks on WD, we observed a 34% increase in atherosclerotic lesions in *Baf60a*^{mKO}/*ApoE*$^{-/-}$ mice ($p = 0.0097$, Figures 1E and 1G). The staining of the aortic root region using hematoxylin and eosin (H&E), oil red O (ORO), and Picrosirius red (PSR) revealed upregulation in lesion ($p = 0.0131$), necrotic core ($p = 0.088$, Figure 1H), lipid deposit ($p = 0.0453$, Figure 1I), and fibrosis ($p = 0.0108$, Figure 1J) in *Baf60a*^{mKO}/*ApoE*$^{-/-}$ mice.

Interestingly, while plasma triglycerides increased in *Baf60a*^{mKO}/*ApoE*$^{-/-}$ mice (Figure S1F), no significant differences were noted in cholesterol content across various lipoproteins, body weight, fasting glucose levels, inflammatory cytokines, or blood cell components (Figures S1B–S1D, S1G, S1H, and S1K). In accordance with no difference in systemic inflammatory cytokines, most inflammatory genes, apart from *Ccl2*, were unaltered in BMDMs isolated from *Baf60a*^{mKO} and 16-week WD-fed *Baf60a*^{mKO}/*ApoE*$^{-/-}$ mice compared to controls (Figures S1I and S1J). The lack of effect on inflammation compared to the previous report by Kong et al.[36] partially suggested the inducible nature of epigenetic architecture, which required specific stimuli and microenvironment to generate context-specific responses.

In exploring the link between *Baf60a* deficiency in myeloid cells and lipid metabolism, we examined the liver and epididymal white adipose tissue (eWAT). No statistically significant alterations were observed in adipocyte hypertrophy, inflammation, or lipid levels in the liver (Figures S2A–S2G). Moreover, inflammatory gene expression and apolipoprotein B levels in the liver were consistent between both groups (Figures S2H and S2I).

Notably, the findings in male mice were repeated in female *Baf60a*^{mKO}/*ApoE*$^{-/-}$ mice, revealing increased atherosclerotic lesions without changes in plasma cholesterol or triglycerides (Figures S2J–S2M). This emphasizes the significance of factors other than systemic lipid levels in atherosclerosis exacerbated by *Baf60a* deficiency in macrophages.

These findings suggest that *BAF60a* is downregulated in advanced atherosclerotic plaque macrophages, and its deficiency exacerbates atherosclerosis in $ApoE^{-/-}$ hypercholesterolemia mice. Moreover, the effect of myeloid BAF60a is mainly vascularly localized and manifests in both male and female sexes.

Myeloid *Baf60a* deletion augments immune cell vascular recruitment

Enhanced inflammation in plaques is a defining trait of atherosclerosis.[37] We observed an upregulation in Mac2-positive macrophage cells in the aortic root of $Baf60a^{mKO}/ApoE^{-/-}$ mice compared to the $Baf60a^{f/f}/ApoE^{-/-}$ group by immunofluorescence ($p = 0.012$, Figures 2A and 2B).

Probing further, we assessed whether BAF60a influences cellular differentiation and maturation. Bone marrow cells from both $Baf60a^{f/f}$ and $Baf60a^{mKO}$ mice were analyzed over time using FACS. There was no significant change in the expression of CD45, CD11b, or F4/80 markers at days 0, 5, and 7 post isolation (Figures 2C and S3A). Additionally, a 5-ethynyl-2′-deoxyuridine (EdU) assay performed on Baf60a-knockdown RAW264.7 cells displayed no shift in DNA synthesis rates (Figure S3B).

Given the notable contribution of circulating monocytes to plaque macrophages,[38] we examined the influence of BAF60a on monocyte adhesion. RNA sequencing (RNA-seq) and gene set enrichment analysis (GSEA) of BMDMs unveiled significant enrichment of high-rank genes related to adhesion upon Baf60a deletion (normalized enrichment score [NES] = 2.025, false discovery rate [FDR] = 0.012, Figures 2D and 2E; Table S2). Furthermore, *Baf60a* deficiency induced upregulation in adhesion-related gene expression, including *Integrin subunit alpha-4* (*Itga4*), *Integrin beta-1* (*Itgb1*), *ST3 beta-galactoside alpha-2,3-sialyltransferase 3* (*St3gal3*), and *Golgi apparatus protein 1* (*Glg1*), which also recapitulated in primary peripheral blood mononuclear cells (PBMCs) (Figures 2F and S3D), THP-1 monocytes (Figure 2G), and day-5 BMDMs (Figure S3E). Moreover, intravital microscopy revealed enhanced leukocyte-endothelium interactions in the $Baf60a^{mKO}/ApoE^{-/-}$ mice post lipopolysaccharide (LPS) injection (Figure S3C).[39] Adhesion assay using THP-1 cells and tumor necrosis factor α (TNF-α)-treated human aortic endothelial cells (HAECs) further showcased heightened monocyte retention with *BAF60a* suppression under activated conditions, but not at baseline (Figures 2H and S3F).

In conclusion, our results underscore the role of BAF60a in modulating cell adhesion, suggesting that its absence intensifies immune cell vascular recruitment.

Baf60a-deficient macrophages exhibit diminished mitochondrial content under pro-atherogenic stress

Mitochondria, essential for oxidative phosphorylation (OXPHOS), are central to macrophage functions, and their dysfunction can exacerbate atherosclerotic plaque formation.[40–45] RNA-seq analyses of BMDMs from mice on a 16-week WD highlighted a pronounced OXPHOS-related gene enrichment in $Baf60a^{f/f}/ApoE^{-/-}$ compared to $Baf60a^{mKO}/ApoE^{-/-}$ mice (NES = 1.627, FDR = 0.004, Figures 3A and 3B; Table S3). This trend manifested as a marked drop in the oxygen consumption rate (OCR) in oxidized LDL (oxLDL)-treated $Baf60a^{mKO}$ BMDMs and in macrophages from $Baf60a^{mKO}/ApoE^{-/-}$

aortas sorted using F4/80 magnetic activated cell sorting (MACS), relative to their respective controls (Figures 3C and 3D).

Mitochondrial DNA (mtDNA) to nuclear DNA (nDNA) ratio, a parameter for examining mitochondrial copy number, revealed diminished mtDNA in oxLDL-exposed *Baf60a*-deficient day-5 and day-7 BMDMs (Figure 3E) and in F4/80^{+} aortic macrophages from atherosclerotic mice, while the non-macrophage counter-part remained unaffected (Figure 3E).

While basal mitochondrial-function-related protein levels—including mitochondrial transcription factor A (mtTFA), cytochrome *c* oxidase (COX IV), pyruvate dehydrogenase complex (PDH), and nuclear respiratory factor 1 (NRF1)—remained stable post *Baf60a* deletion (Figure S4A), an oxLDL challenge precipitated a decrease in the protein levels of mtTFA, COX IV, and PDH in *Baf60a*-deficient BMDMs (Figure 3F). This underscores the pivotal role of the atherosclerotic environment in potentiating mitochondrial anomalies upon *Baf60a* loss.

Atherosclerotic signals exacerbate mitochondrial dysfunction, reactive oxygen species production, and apoptosis in *Baf60a*-deficient macrophages

Oxidatively modified lipoproteins such as oxLDL are integral to the intricate microenvironment in plaque.[46] While *Baf60a* deficiency diminishes mitochondrial proteins during oxLDL exposure, it remains unaffected at basal levels. We hypothesize that oxLDL-induced stress precipitates BAF60a-related mitochondrial dysfunction in BMDMs.

Transmission electron microscopy (TEM) imaging of *Baf60a*-deficient BMDMs treated with oxLDL (100 μg/mL, 48 h) showed a decline in mitochondrial count ($p = 0.0307$) and a surge in autophagosomes encapsulating deteriorating mitochondria ($p < 0.0001$, Figure 4A) compared to the control. The depolarized mitochondrial membrane potential and enhanced proton leak, indicative of mitochondrial dysfunction, elevate reactive oxygen species (ROS) associated with mitochondria, exemplified by increased MitoSOX accumulation, which was heightened in *Baf60a*-deficient BMDMs under oxLDL exposure (50 μg/mL, 48 h, Figures 4B and 4D) and was independent of lipid-uptake alterations (Figures 4C and S4B–S4D).

Persistently impaired mitochondria can instigate autophagy and, eventually, apoptosis. Recognized for inciting macrophage damage during atherosclerosis, the primary oxysterol constituent of oxLDL, 7-keto cholesterol (7-KC),[47,48] was investigated. After a 24-h exposure to 10 μg/mL 7-KC, *Baf60a*^{mKO} BMDMs displayed elevated damage-associated lactate dehydrogenase (LDH) release (Figure 4E) and a rise in annexin V-positive/propidium iodide (PI)-negative apoptotic cells (Figure 4F) when compared to controls.

In vivo analyses substantiated these observations. Mac2 and TUNEL co-staining pinpointed an amplified apoptosis signal overlaying the plaque macrophage region upon *Baf60a* deficiency (Figure 4G). Likewise, MACS-sorted F4/80^{+} aortic macrophages from the *Baf60a*^{mKO}/*ApoE*$^{-/-}$ atherosclerotic mouse model also showed an increase of MitoSOX, annexin V, and PI signals compared to *Baf60a*$^{f/f}$/*ApoE*$^{-/-}$ macrophages, and a decrease of mitochondria membrane potential sensitive tetramethylrhodamine (TMRM) signal compared

to the aortic macrophages from control mice (Figure S4D). Moreover, adenovirus-induced *BAF60a* overexpression alleviated atherosclerotic-triggered mitochondrial ROS (Figure S4E), LDH release (Figure S4F), and cellular apoptosis (Figure S4G).

Correlation of *BAF60a* expression and mitochondrial gene expression in plaque macrophages from human subjects

As a chronic inflammatory and progressive disease, the intrinsic plasticity and heterogeneity of the plaque environment confer drastic plasticity to the plaque macrophage populations.[37,38] Historically, membrane protein expression-based analyses have delineated a minimum of eight atherosclerosis-associated macrophage subtypes with diverse functional roles, including inflammation propagation, phagocytosis, lipid metabolism, and plaque repair.[37,49–56] More recent techniques utilizing single-cell transcriptomics, CyTOF (cytometry by time of flight), and CITE-seq (cellular indexing of transcriptomes and epitopes by sequencing) divide plaque macrophages into four major clusters: inflammatory, resident-like, interferon (IFN)-induced, and triggering receptor expressed on myeloid cells 2 (TREM2) foamy macrophages.[38,57–62]

Having observed exacerbated atherosclerosis and mitochondrial dysfunction under pro-atherogenic conditions in *Baf60a*^{mKO} mice, we hypothesized a similar regulatory mechanism potentially underlying plaque formation and macrophage plasticity in humans. Pursuing this hypothesis, we reevaluated published single-cell RNA-seq (scRNA-seq) data (GEO: GSE159677),[63] comprising 51,721 cells from three atherosclerotic plaque samples and their matched controls. A rigorous quality control and normalization process ensued, followed by an unsupervised shared nearest neighbor-based clustering to categorize cell types.[64] This analysis, when focused on macrophages, uncovered 14 distinct clusters with four identified macrophage subtypes, labeled Mφ1 through Mφ4 (Figures 5A, 5B,and S5A). Although *BAF60c* expression was predominant in smooth muscle cells, *BAF60a* and *BAF60b* expressions spanned across various cell types. Notably, within the macrophage subsets, the Mφ4 cluster predominantly showed elevated *BAF60a* expression, while Mφ3 was presented with relatively lower levels (Figures 5A and S5B).

Pathway enrichment analysis of macrophage subpopulations using gene ontology (GO) and the Kyoto Encyclopedia of Genes and Genomes (KEGG) further illuminated the functional implications of these differences. Mφ4 macrophages, which expressed *BAF60a* at high levels, exhibited a surge in chromatin-remodeling-related genes, hinting at potential BAF60a-driven chromatin activities (Figures 5C and S5D). Conversely, the Mφ3 subset, characterized by lower *BAF60a* levels, displayed upregulated genes governing cell communication and adhesion (Figures 5C and S5D)—an observation aligning with the heightened immune cell recruitment and monocyte adhesion in *Baf60a*-deficient mice.

Drawing parallels between human and murine macrophage populations, we discerned the human Mφ1 cluster to exhibit attributes resonating with inflammatory, IFN-induced, and resident-like macrophage signatures from mice (Figure S5E). The Mφ2 subset closely mirrored the TREM2-high foamy cell profile. Intriguingly, Mφ3 and Mφ4, constituting approximately a quarter of the macrophage population, demonstrated distinctive transcriptional attributes from the primary macrophage clusters found in

plaques, particularly marked by differential expression of genes governing mitochondrial functionality and OXPHOS (Figure 5D).

Broadening our analytical scope to address potential variabilities arising from limited sample sizes, we employed deconvolution on 126 bulk human plaque microarray samples sourced from the Biobank of Karolinska Endarterectomy using single-cell gene expression as the reference matrix (Figure S5F).[65] The analysis depicted a robust positive association between BAF60a expression and Mφ4 prevalence ($\beta = -0.455$, $p = 0.042$) and an inverse relationship with Mφ3 abundance ($\beta = 0.461$, $p = 0.002$, Figure 5E). Collectively, our findings fortify the role of BAF60a as a potential pivotal regulator in orchestrating plaque macrophage mitochondrial dynamics, immune response modulation, phenotype switching, and the overarching progression of atherosclerosis.

Baf60a deficiency alters NRF1 transcriptional dynamics in response to atherosclerotic stress and attenuates NRF1-regulated gene activity

BAF60a is recognized for its pivotal role in modulating gene expression by orchestrating its interactions with TFs and influencing the specific recruitment of the SWI/SNF complex to select genomic locales.[34] To demystify the underlying molecular processes responsible for the mitochondrial dysfunction linked to Baf60a deficiency, we performed an assay for transposase-accessible chromatin sequencing (ATAC-seq). This was performed on cells derived from oxLDL-exposed (50 μg/mL for 48 h) BMDMs from *Baf60a*^{mKO}/*ApoE*$^{-/-}$ and *Baf60a*$^{f/f}$/*ApoE*$^{-/-}$ mice. Our results showcased that *Baf60a* deficiency does not alter overall chromatin accessibility (Figure S6A), yet it does reduce the number of discerned peaks within the 3-kb promoter region (Figure 6A).

Exploration of the transcriptional footprint revealed changes to various TF activities in response to atherogenic conditions and *Baf60a* absence (Figure 6B). Intriguingly, the footprint of NRF1—a TF governing mitochondrial biogenesis—was heightened under oxLDL exposure (Figure S6C) but substantially repressed upon *Baf60a* removal (Figures 6C and S6B–S6D). Concurrently, *Baf60a* depletion in oxLDL-challenged BMDMs (50 μg/mL for 48 h) did not modify the transcriptional dynamics of well-known BAF60a-interacting or regulatory TFs, such as ATF3, and PGC1α-regulated ESRRA or PPARG (Figure S6D),[10,33,36,66] emphasizing the context-dependent behavior of BAF60a. Additionally, HOMER motif enrichment analysis distinctly highlighted an under-representation of NRF1 in *Baf60a*^{mKO} macrophages compared to the control (Figure 6D).

Using a genome browser, we juxtaposed signals from ATAC-seq with data from previously reported Nrf1 chromatin immunoprecipitation sequencing (ChIP-seq) (GEO: GSE208936) and Brg1, H3K27ac, and H3K4me1 CUT&RUN sequencing (CUT& RUN-seq) (GEO: GSE192777) on the promoter region of NRF1 target genes. Specifically examining *Tfb1m*, we noticed congruence between ATAC-seq chromatin-accessible regions and NRF1 TF binding sites, which receded in the context of *Baf60a* deficiency. This points toward the synergistic involvement of BRG1 and histone modification in the TF binding processes (Figure 6E). Subsequent ChIP assays corroborated the reduced affinity of both NRF1 and BRG1 to anticipated promoter regions in *Tfb1m*, specifically within the chr17:3,557,648–3,557,842, mm10 segment (Figure 6F). Furthermore, we identified that the absence of

Baf60a precipitated the downregulation of NRF1-influenced gene transcription pertaining to mitochondrial dynamics. This encompasses primary NRF1 targets as well as secondary downstream targets in the pathway, notably Mitochondrial transcription *factor-A* (*Tfam*), -*B1* (*Tfb1m*), and -*B2* (*Tfb2m*), *Heat shock protein family D member 1* (*Hspd1*), and *Pyruvate dehydrogenase E1 subunit alpha 1* (*Pdha1*). However, *Nrf1* expression remained unaffected (Figure 6G). Collectively, these findings underscore the instrumental role of BAF60a in safeguarding mitochondrial functionality through its interaction with NRF1, thereby facilitating chromatin accessibility at critical mitochondrial-associated genes.

BAF60a interacts with NRF1, and its overexpression relies on NRF1 to rectify mitochondrial impairment

We noted a direct physical bond between BAF60a and NRF1, underscoring their intertwined functionality (Figures 7A and S7A). Additionally, this interaction appears direct, without the mediation of the transcription co-factor Pgc1a (Figure S7B).

Seeking insights into whether repairing the compromised epigenetic-metabolic crosstalk can rectify macrophage anomalies, we probed: (1) the extent to which *Baf60a* ablation suppresses NRF1-driven mitochondrial biogenesis; and (2) the underlying mechanism by which *BAF60a* affords protection to macrophages under atherosclerotic conditions.

For this purpose, RAW264.7 cells were subjected to transfection with siNT/siBaf60a and pcDNA/NRF1 through nucleofection, followed by exposure to control or oxLDL conditions (50 μg/mL for 24 h, Figure 7B). Our observations revealed that the upregulation of NRF1 ($p = 0.0001$) considerably mitigated the dip in mitochondrial-associated proteins, notably COX IV ($p = 0.0008$) and mtTFA ($p = 0.0205$, Figure 7C), in *Baf60a*-deficient macrophages upon oxLDL stimulation. Furthermore, the protective role offered by BAF60a against the decline of mitochondrial-centric genes in oxLDL-exposed *Baf60a*^{mKO} BMDMs was reduced upon downregulating the key macrophage SWI/SNF ATPase unit, BRG1. This protective effect was entirely neutralized with *NRF1* depletion (Figure 7D). Notably, we also detected an increased defense against mtDNA decrease either by re-establishing *Baf60a* expression ($p < 0.0001$, Figure 7E) or by amplifying *NRF1* levels ($F(2,27) = 31.1$, $p = 0.0072$, Figure 7E).

DISCUSSION

Our study revealed the critical role of BAF60a-mediated chromatin remodeling in protecting macrophages under atherogenic stress. Specifically, we have found that the interaction between BAF60a and NRF1 is crucial for maintaining a physiological level of mitochondrial function in macrophages. However, this interaction is likely disrupted in plaque macrophages when the NRF1-dependent adaptive response machinery is activated, but BAF60a-dependent chromatin accessibility is reduced due to exacerbated atherosclerotic stress and its associated factors, causing a reduction in *BAF60a*. The dysregulation disrupts mitochondrial biogenesis, leading to increased ROS leakage, macrophage apoptosis, and further plaque progression (Figure 7E).

Epigenetic modifications and chromatin remodeling have been linked to various physiological and disease-associated conditions that regulate differential gene expression in

response to disease progression.[67] Understanding the coordination of environmental factors that alter chromatin structure and gene expression in the context of vascular diseases and their crosstalk with cells in the vasculature is crucial for identifying therapeutic targets for CVDs. This is especially relevant in atherosclerosis, considering the high residual risks for current therapy that mainly focuses on classical lipid profile, inflammation, and lifestyle management. To date, four major ATP-dependent chromatin remodeler families have spiked the highest study interest, SWI/SNF, ISWI, CHD, and INO80, with SWI/SNF being the largest, most multifunctional, and evolutionarily conserved complex.[68]

The SWI/SNF chromatin remodeling complex represents a class of multiunit complexes connecting to various genomic positions, including distal enhancers, promoters, and CTCF binding sites, where they facilitate and maintain DNA accessibility to control gene transcription and are often associated with transcriptional activation.[69] Changes in SWI/SNF ATPase subunits BRG1 and BRM have been linked to the primary and secondary responses to stress in BMDMs through alterations of chromatin accessibility.[70,71] BAF60s are unique among all the SWI/SNF subunits, since they operate as a bridge connecting the SWI/SNF complex and specific TFs.[72] The differential controls exerted by BAF60s in the context of metabolic and inflammatory diseases have been demonstrated in previous studies, including ours.[10,11,33–36,73] In the present work, we solved the puzzle of how *BAF60a* controls macrophage metabolic homeostasis in atherosclerosis. We showed that the expression of Baf60a is downregulated in macrophages during advanced atherogenesis and confirmed that myeloid *Baf60a* deletion exacerbates atherosclerosis plaque formation in mice at least partially through induction of mitochondrial dysfunction.

The mitochondrion is the primary powerhouse of most cells, including macrophages.[41] Fatty acids, amino acid metabolites, and pyruvate derived from glycolysis enter the tricarboxylic acid cycle in the mitochondrial matrix, which carries protons to the electron transport chain, producing chemical gradients at the intermembrane spaces that generate ATP in a process known as OXPHOS. Changes in the microenvironment that shift the mitochondria energy balance between OXPHOS and glycolysis have been closely linked to different macrophage subtypes and functions in inflammatory and metabolic diseases such as atherosclerosis.[42–44,74–77] Conversely, changes in macrophage metabolism and epigenetic modifications have been proposed to alter macrophage phenotype and are potentially associated with disease conditions. Recent research has uncovered that atherosclerotic plaque has a complicated metabolic milieu, and it has been reported that cells within the unstable plaque have a higher glycolysis rate, increased amino acid utilization, and suppressed fatty acid oxidation compared to stable plaques.[78] In alignment with the previous observation between BAF60a and macrophages portraying high expression of mitochondrial-related genes, we report robust mitochondrial dysfunction upon *Baf60a* deletion through a series of *in vitro* and *in vivo* functional and structural assays. Moreover, we identified that mitochondrial dysfunction occurs when the cell senses the atherosclerotic environmental cues and further induces cell toxicity and apoptosis which, as a result, is known to promote advanced plaque necrosis directly.[79,80]

As a chronic inflammatory and progressive disease, the complex microenvironment of the atherosclerotic plaque assigns drastic plasticity to the plaque immune cell populations,

especially macrophages.[38] Despite the initial observation that a binary categorical classification of LPS/INF-γ-induced pro-inflammatory M1 macrophages and interleukin-4 (IL-4)/IL-13-induced anti-inflammatory M2 macrophages exist and seemingly align well with the responses to T helper 1 (Th1) and Th2,[81] continuous evidence has proved that there is often a lack of clearly defined corresponding subsets *in vivo*. Furthermore, the binary classification overlooks the complexity of pathological situations.[37,82] There have been macrophage subtype disparities overwhelmingly reported in atherosclerosis and CVDs, as recently reviewed.[38] However, the major determinants for their polarization/differentiation and how these diverse subpopulations contribute to atherosclerosis are poorly understood. By reanalyzing publicly available human plaque scRNA-seq data and applying it to deconvolute cell composition in the human plaque microarray results, we report a positive association between *BAF60a* and the Mφ4 population, which showed a high level of expression of mitochondrial-related genes and a negative association between *BAF60a* and the Mφ3 population, which is enriched in genes related to cell-cell communication and adhesion. Our results suggest the potential involvement of BAF60a in plaque macrophage diversity and establish its predictive roles in regulating mitochondrial function and immune cell adhesion in both human and mouse atherosclerosis.

Morphological and functional alterations in mitochondria are precisely controlled by a group of TFs, including NRF1, the master regulator of mitochondrial biogenesis.[83] In smooth muscle cells NRF1 participates in the synthesis of miR-378a, and its deficiency induces smooth muscle synthetic phenotype contributing to atherosclerosis.[84] In patients, the expression of *NRF1* and its downstream target *TFAM* were decreased in carotid atherosclerotic plaques.[85] Additionally, specific *NRF1* polymorphisms (rs12706898T and rs1882094T allele) were associated with an increased risk of ischemic stroke, a major event of ruptured atherosclerosis.[86] However, the function of NRF1 in plaque immune cells and their contribution to atherosclerosis remain elusive. The present work points to the contribution of macrophage NRF1 in atherosclerosis. We found that mechanistically, *Baf60a* deficiency reduces the NRF1 binding to essential mitochondrial-related genes under atherosclerotic stress. This regulation is likely through a physical interaction between BAF60a and NRF1, as evidenced by the co-IP assay between NRF1 and intact/truncated BAF60a. As a result, we confirmed that restoring the disrupted epigenetic-metabolic crosstalk through *BAF60a* overexpression rescues macrophage mitochondria loss in an NRF1-dependent manner, while overexpression of *Nrf1* also functionally compensates for the mitochondrial dysfunction caused by the loss of *Baf60a*.

Interestingly, it is increasingly apparent that the role of SWI/SNF complex and BAF60a in various disease conditions is highly context dependent. For example, recent research showed that *Baf60a* decreased in the white adipose tissue macrophage (ATM) of diabetic mice.[36] Its deficiency induced the pro-inflammatory activation of ATM due to disrupted interaction between BAF60a and ATF3 and caused obesity and diabetic syndrome.[36] In contrast, in the context of atherosclerotic stress, we found that aortic macrophages, although showing reduced OXPHOS, resemble neither classical activated M1 nor alternative activated M2 macrophage gene signatures, and oxLDL-treated *Baf60a* deficiency BMDMs also showed no changes in ATF3 activities. It is worth noting that macrophages express high levels of *ApoE*, which is not only a primary component of lipoproteins but is also renowned for

its anti-inflammatory properties.[87] Therefore, the absence of inflammation-related effects linked to BAF60a and ATF3 might be influenced, at least in part, by the background of *ApoE* deficiency. This aspect should be thoroughly examined in future studies by additional experiments including bone marrow transplantation and utilizing mice in *LDLR*-deficient background.

In conclusion, we identified that BAF60a is required for macrophage mitochondrial energy homeostasis under pro-atherosclerotic stress by preserving adaptive NRF1 accessibility to essential nuclear mitochondrial genes in an SWI/SNF-complex-dependent way. Our results suggest that targeting mitochondrial homeostasis and restoring physiological epigenetic-metabolic crosstalk may hold great potential for treating diseases such as atherosclerosis.

Limitations of the study

We studied the role of BAF60a in regulating cell adhesion, suggesting heightened immune cell recruitment upon its deficiency. The precise interplay between NRF1 and BAF60a, particularly its impact on monocyte adhesion, remains to be elucidated in detail. Meanwhile, a recent work by Kong et al. illuminated the role of BAF60s, especially BAF60a, in ATM activation tied to obesity and metabolic inflammation.[36] Questions are raised about whether and to what extent metabolic shifts from BAF60a deficiency contributed to its influence on atherosclerosis. Additionally, the inherent exclusivity of the three BAF60 subunits within the SWI/SNF complexes underscores the need for a deeper understanding of how these individual BAF60 subunits orchestrate and co-function during disease progression. Furthermore, to a broader extent, the mammalian SWI/SNF complex subunits converge to form three distinct BAF complexes: the canonical BAF, polybromo-associated BAF, and non-canonical BAF complexes.[32] The relative abundance of these complexes in different cell types and their preferential activity in atherosclerosis and other cardiovascular diseases remain pivotal questions that are largely unaddressed. To conclude, the multifaceted role of BAF60a across a spectrum of disease conditions and its intricate downstream regulatory pathways, including its interaction with NRF1, present numerous potential therapeutic opportunities. However, the transition from controlled *in vitro* findings to the dynamic realm of *in vivo* applications, particularly in the context of targeted therapeutic strategies, remains a challenging endeavor that requires sophisticated refinements in future investigations.

STAR★METHODS

RESOURCE AVAILABILITY

Lead contact—Further information and requests for resources and reagents should be directed to and will be fulfilled by the Lead Contact, Jifeng Zhang (jifengz@umich.edu).

Materials availability—All unique/stable reagents generated in this study are available from the lead contact with a completed Materials Transfer Agreement.

Data and code availability

- The raw reads and processed data pertaining to RNA-Seq and ATAC-Seq are accessible via the Gene Expression Omnibus database (GEO) under accession

number GSE224668. Pre-existing scRNA-Seq, ChIP-Seq, and CUT&RUN-Seq data from prior publications are accessible via GSE159677,[63] GSE192777,[96] and GSE208936,[97] respectively. Raw data has been deposited at Mendeley (https://doi.org/10.17632/2v6vfjw8j4.1).

- This paper does not report original code.
- Any additional information required to reanalyze the data reported in this paper is available from the lead contact upon request.

EXPERIMENTAL MODEL AND STUDY PARTICIPANT DETAILS

Animal studies—C57BL/6J background *Baf60a* floxed (*Baf60a*$^{f/f}$) mice[34] maintained in lab were crossbred with *ApoE*$^{-/-}$ (B6.129P2-*ApoE*$^{tm1Unc/J}$) and Lyz2Cre (B6.129P2-Lyz2$^{tm1(cre)Ifo/J}$) mice purchased from the Jackson Laboratory to generate the *Baf60a*^{mKO}/*ApoE*$^{-/-}$ and *Baf60a*$^{f/f}$/*ApoE*$^{-/-}$ littermate control. All mice were kept on a regular 12h light/12 h dark cycle at 22°C in a pathogen-free environment. Mice at 10 to 12-week-age were fed a high-cholesterol Western diet, referred to as WD (Envigo, TD.88137) to induce hypercholesterolemia for an additional 8, 12, or 16 weeks, varying by experiments. Both male and female sexes were used in the study and specified in the figure legends. All animal procedures protocols were approved by the Institutional Animal Care & Use Committee at the University of Michigan.

Cell culture—Bone marrow cells were harvested from the femur and tibia of mice aged 6 to 12 weeks. These cells were then cultured in differentiation medium (comprising 10% FBS Gibco IMDM, 1X Non-Essential Amino Acids, 1mM Sodium Pyruvate, and 20 ng/mL M-CSF) for a duration of up to 7 days to facilitate their differentiation into Bone marrow-derived macrophages (BMDMs) and then transferred to standard 10% FBS DMEM. THP-1 cells were purchased from ATCC and cultured in RPMI1640 with 10% FBS. RAW264.7 cells were purchased from ATCC and cultured in DMEM with 10% FBS. Human aortic endothelial cells (HAECs) were purchased from Lonza and cultured in EC growth media-2 from passages 4 to 8. AD-293 cells were purchased from Agilent and cultured in DMEM with 10% FBS.

METHOD DETAILS

Histology—After euthanasia, mice were perfused with ice-cold saline through the left ventricle. Aortic root, liver, and eWAT tissue were dissected, fixed in formalin, embedded in paraffin or frozen OCT, followed by sectioning. The H&E Staining, Oil Red O, Picro Sirius Red Stain, and F4/80 immunohistochemistry were performed by the *In-Vivo* Animal Core (IVAC) at the University of Michigan. For the TUNEL assay, paraffin-embedded aortic sections were stained using the ApopTag Peroxidase *In Situ* Apoptosis Detection Kit (Millipore Sigma, S7100). In addition, en-face staining of the whole aorta was conducted through excising the aorta from the heart to the iliac bifurcation, removing adventitial tissue, and staining with ORO before imaging.[98] Lobular inflammation was quantified using FILP algorithm.[99] Quantification of histological staining was done using ImageJ.

Lipoprotein fractionation and quantification—Fast protein liquid chromatography (FPLC)[17] was used to determine the amount of cholesterol contained in specific lipoprotein particle fractions. Pooled fasting plasma from all *Baf60a*^{mKO}/*ApoE*$^{-/-}$ and *Baf60a*$^{f/f}$/*ApoE*$^{-/-}$ mice was eluted into 40 fractions. Cholesterol content in all fractions were analyzed using a cholesterol fluorometric test kit (Cayman Chemical, 10007640).

Plasma lipid, glucose, and complete blood count (CBC)—Fasting plasma total cholesterol (TC) and triglyceride levels were measured using a colorimetric-based assay (Fujifilm Wako Diagnostics, 999–02601 and 290–63701). Fasting blood glucose was measured using a glucometer and glucose test strips (Ascensia, 0193–7308-50). CBC was performed by the IVAC at the University of Michigan.

Isolation of mouse peripheral blood mononuclear cells (PBMCs)—Fresh blood was collected into BD Microtainer Tubes with K2EDTA, mixed immediately to prevent aggregation and further supplemented with 20 μL of 0.5M EDTA. The blood was then diluted with an equal volume of DPBS. This diluted sample was carefully layered over 3 mL of Ficoll-Paque media in a 15 mL centrifuge tube and centrifuged at 400 g for 30–40 min at 18°C–20°C without braking. The plasma-containing upper layer was removed, leaving the mononuclear cell layer undisturbed. The mononuclear cells were then transferred to a sterile centrifuge tube, diluted with three volumes of DPBS, and resuspended by gentle pipetting. After centrifugation at 400–500 × g for 10–15 min at 18°C–20°C, the supernatant was discarded and cells were resuspended in 3 mL of balanced salt solution. For further RBC removal, 1 mL RBC lysis buffer was added, incubated for 10 min at room temperature, and halted with 10 mL balanced salt solution. After another centrifugation round, the cell pellet was resuspended in suitable media for CD11b MACS enrichment.

Lipid extraction from liver—Immediately after procurement, tissues were weighed, homogenized, and mixed with a chloroform and methanol solution in a 2:1 ratio, using 20μL of this solvent mixture per 1mg of tissue. This mixture was then centrifuged at 2400 rpm for a duration of 5–10 min. Lipid-enriched supernatant was carefully decanted into a fresh tube. Next, double-distilled water, amounting to 0.2 times the volume of the original solution, was added to the supernatant and mixed thoroughly. Following another round of centrifugation at 2400 rpm for 5–10 min, the aqueous and organic phases were segregated. The organic phase, constituting the bottom layer and containing the extracted lipids, was collected, ensuring an upper to lower layer volume ratio of about 2:3. The organic phase was then dried with gentle heating at 37°C and redissolved in a suitable volume of assay buffer for lipid detection.

Western blot (WB)—Tissue or cells were lysed in RIPA buffer (Thermo Fisher Scientific, 89901) with protease inhibitor (Roche, 11873580001). Protein extracts were resolved in SDS-PAGE gels and transferred to nitrocellulose membranes. Membranes were blocked with 5% milk or BSA for 1 h at room temperature, followed by incubation with primary antibody (4°C overnight) and then fluorescence-labeled secondary antibody (Li-Cor Bioscience, 1:5,000 to 10,000 dilution) at room temperature for 1–2h. The membrane was

scanned using the LI-COR DLx Odyssey imaging system. Quantification was performed using LI-COR Empiria Studio.

Quantitative real-time PCR (qPCR)—Total RNA from tissue was first purified using TRIzol (Invitrogen, 15596018) and RNeasy Mini Kit (Qiagen, 74106). mRNA from cells was isolated using RNeasy Mini Kit directly. mRNA was reverse transcribed with SuperScript III kit (Thermo Fisher Scientific, 18080051) using random hexamer. cDNA abundance was measured in BioRad Real-time PCR Detection System, using SYBR Green Fast qPCR Mix (Abclonal, RK21203). Unless otherwise specified, gene expression level was normalized to the internal control, GAPDH. qPCR primers are listed in Table S1.

Plasma cytokine enzyme-linked immunosorbent assay (ELISA)—Plasma MCP-1 and IL-6 levels in *Baf60a*^{mKO}/*ApoE*$^{-/-}$ mice and *Baf60a*$^{f/f}$/*ApoE*$^{-/-}$ mice were measured by the Cancer Center Immunology Core at the University of Michigan.

Aortic cell digestion followed by fluorescence-activated cell sorting (FACS) or magnetic-activated cell sorting (MACS)—Mice were euthanized and perfused with ice-cold PBS containing 2% heparin through the left ventricle. Aortas were digested in a cocktail of 450 U/mL collagenases (Gibco, 17100–017 and Sigma-Aldrich, C7657), 60 U/mL hyaluronidase (Sigma-Aldrich, H3606), and DNase-I (Roche, 10104159001, 37°C, 90 min).[100] Suspensions were filtered by a 100 μm cell strainer to isolate single cells. 1) For FACS: Cells were further blocked in Fc blocker (eBioscience, 14–0161-85) for 5 to 10 min on ice and then incubated with fluorochrome-conjugated antibodies for additional 30 min. Cells were fixed and sent to the Flow Cytometry Core at the University of Michigan.[100] Antibodies used for flow cytometry were as follows: CD16/CD32 for Fc blocking (eBioscience, 14–0161-85), eFluor 450 isotype control (rat IgG2b kappa, eBioscience, 48–4031-82), APC conjugated isotype control (rat IgG2a kappa, eBioscience, 17–4321-81), PerCP-cy5.5 isotype control (eBR2a, eBioscience, 45–4321-80), FITC isotype control (Biolegend, 400110), APC-Cy7 isotype control (BioLegend, 400623), eFlour 660 isotype control (rat IgG2a Kappa, eBioscience, 50–4321-82), CD45 (EF450, eBioscience, 48–0451-82), Mac2 (EF660, eBioscience, 50–5301-82), Ly6G (FITC, BioLegend, 127605), F4/80 Rat anti-mouse (APC, TONBO 130–102-471), CD11b (APC-Cy7, BioLegend, 101225), CD19 (FITC, BD Biosciences, 557398), CD3 (PerCP-Cy5.5, eBioscience, 45–0031). 2) For MACS: Single aortic cells were passed through anti-F4/80 (130–110-443), or anti-CD11b MicroBeads (130–049-601) from Miltenyi Biotec (Gaithersburg, MD) following the manufacturer's protocol. Macrophages and flowthrough control cells were either cultured in Seahorse medium for OCR assay, used for quick DNA extraction, or stained with Mac2 (EF660, eBioscience, 50–5301-82) and other fluorescent indicators. FACS data were analyzed using FlowJo v10.6.1.

Cell adhesion assay—HAECs at confluence were treated with TNFa (2 ng/mL) for 6h, followed by washing with PBS and re-culturing in Opti-MEM medium (Gibco, 31985062) for an additional 10h. THP-1 with siControl or siBAF60a were stained with 1uM Calcein A/M and seeded onto the HAECs for 5h. The cells were washed with cold PBS three times, stained with NucBlue (Thermo Fisher Scientific, R37605), and visualized using

a fluorescent microscope (Keyence, BZ X800). The retention rate was quantified by normalizing the Calcium A/M positive area post-washing to the prewashing area in each well. Fiji ImageJ analyzer was used for quantification.

Nucleofection of siRNAs and plasmids—Nucleofection of siRNAs (30–50 nM) and plasmids in macrophages were performed in a Nucleofector 2b Device, using Human Monocyte Nucleofector Kit (VPA-1007) and Nucleofector Program Y-001, for 1×10^6 to 2×10^7 cells per 100μL transfection solution.

Leukocyte adhesion—Eight weeks old male *Baf60a*^{mKO} and *Baf60a*$^{f/f}$ mice were IP injected with 50 μg/kg LPS. Four hours later, mice were injected with rhodamine 6G chloride to label the leukocyte population. After anesthetization, the cremaster muscle was separated from the tissues around it. Intravital microscopy was used to track the leukocyte movement and took illustration pictures.[101]

Oxygen consumption rate measurement by seahorse—Agilent Seahorse XFe96 Analyzer was used to measure the oxygen consumption rate (OCR). F4/80+ aortic macrophages isolated from the *Baf60a*^{mKO}/*ApoE*$^{-/-}$ and *Baf60a*$^{f/f}$/*ApoE*$^{-/-}$ mice, and BMDMs from *Baf60a*^{mKO} and *Baf60a*$^{f/f}$ mice were cultured in the 96-well culture plates. The sequential administration of drugs occurred as follows: A) 10 mM glucose +1 mM sodium pyruvate; B) 1 μM oligomycin; C) 2 μM FCCP; and D) 0.5 μM rotenone +0.5 μM antimycin A.

Mitochondrial DNA copy number—F4/80$^+$ aortic macrophages isolated from the *Baf60a*^{mKO}/*ApoE*$^{-/-}$ and *Baf60a*$^{f/f}$/*ApoE*$^{-/-}$ mice, and BMDMs from *Baf60a*^{mKO} and *Baf60a*$^{f/f}$ mice were digested with proteinase K. Genomic (nDNA, B2M), and mitochondrial DNA (mtDNA) were extracted using Phenol:Chloroform: Isoamyl Alcohol (25:24:1,v/v, Thermo Fisher Scientific, 15593049). The aqueous phase was further purified in cold 70% ethanol. mtDNA to nDNA ratio numbers were quantified by qPCR, using B2M and mtDNA specific primers listed in Table S1.[17]

Transmission electron microscopy (TEM)—BMDMs from *Baf60a*^{mKO} and *Baf60a*$^{f/f}$ mice were treated with oxLDL (100μg/mL) for 48 h in DMEM, followed by fixation and TEM imaging in the Microscopy Core of the University of Michigan.

Annexin V/PI assay—BMDMs from *Baf60a*^{mKO} and *Baf60a*$^{f/f}$ mice were treated with 7-KC (10μg/mL, 24 h) in Opti-MEM medium (Gibco, 31985062). The cells were first dissociated with 0.25% trypsin and stained with the FITC Annexin V Apoptosis Detection Kit I (BD Biosciences, 556547). In general, the cells were washed with cold PBS, followed by suspension in a 1x binding buffer, and then labeled with FITC Annexin V and Propidium Iodide (PI) for 10 to 15 min at room temperature.[101] Quantification was done by FACS at the University of Michigan core facility.

Lactate dehydrogenase (LDH) activity assay—BMDMs from *Baf60a*^{mKO} and *Baf60a*$^{f/f}$ mice were treated with 7-KC (10μg/mL) for 24 h in Opti-MEM medium. LDH assay was performed using the LDH kit (MAK066) from Sigma-Aldrich.

Cell and mitochondrial staining—BMDMs from *Baf60a*^{mKO} and *Baf60a*$^{f/f}$ mice were treated with oxLDL (50μg/mL) for 48 h in DMEM, followed by staining with 1X working concentration MitoTracker Deep Red FM (M22426), MitoSOX Red (M36008), HCS LipidTOX Green (H34475), NucBlue, or TMRM (T668) from Thermo Fisher Scientific. Cells were visualized using a fluorescent microscope (Keyence, BZ X800) and quantified by FACS in the Flow Cytometry Core at the University of Michigan. Data were analyzed using FlowJo v10.6.1.

Co-immunoprecipitation assay—Co-immunoprecipitation (Co-IP) assays were performed by lysing RAW264.7 cells or Ad293 cells using Cell Lysis Buffer (CST, 9803) supplemented with PMSF (CST, 8553). Immunoprecipitation was achieved by incubating the lysate with Protein G Magnetic Beads (CST, 7024) or antibodies against HA or antibodies against HA (ABclonal-AE008 for RAW264.7 cells or CST-3724 for Ad-293 cells) overnight at 4°C with rotation. The pellet was resuspended in SDS sample buffer and heated to 95°C–100°C for 5 min. The supernatant, comprising the sample, was isolated for next-step Western blot assay.

RNA sequencing (RNA-Seq) analysis—RNA was collected from BMDMs of either *Baf60a*^{mKO} and *Baf60a*$^{f/f}$ mice or after 16-week WD feeding of *Baf60a*^{mKO}/*ApoE*$^{-/-}$ and *Baf60a*$^{f/f}$/*ApoE*$^{-/-}$ mice using the procedure as described for qPCR, and treated with RNase-free DNase I (QIAGEN, 79254) at room temperature for 10 min before sequencing. RNA was sent to the advanced genomic core at the University of Michigan for library preparation and sequencing. DeSeq2[94] tool was used to perform differential expression analysis. In addition, GO and KEGG enrichment analyses were performed using GSEA v4.3.2.

Single-cell RNA sequencing (scRNA-Seq) analysis—Single-cell RNA sequencing (scRNA-seq) data of 51,721 cells from three human atherosclerotic plaque samples and matched controls was extracted from GSE159677 and followed by QC, normalization, clustering, and generating expression matrix using Seurat 4.0.[64] GO and KEGG analysis were performed using ClusterProfiler.[95] Cell type deconvolution was performed in CIBERSORTx.[65] The microarray of 126 bulk human plaque samples was from the Biobank of Karolinska Endarterectomy (BiKE).

Chromatin immunoprecipitation (ChIP) assay and transposase-accessible chromatin using sequencing (ATAC-Seq) assay—BMDMs from *Baf60a*^{mKO}/*ApoE*$^{-/-}$ and *Baf60a*$^{f/f}$/*ApoE*$^{-/-}$ mice were treated with vehicle control or oxLDL (50μg/mL, 48 h). For ChIP assay, chromatin regions were immunoprecipitated with antibodies against BRG1(Abcam, ab110641)[10] and NRF1 (Thermo Fisher Scientific, PA5–27854) followed by qPCR analysis. ATAC-Seq of nuclei isolated from the cell was performed by the Epigenomics Core at the University of Michigan and CD Genomics. After quality control (FastQC)[92] and alignment to the corresponding genome (Bowtie2,[88] mm10), bam files were indexed and filtered against the blacklist region using Samtools.[89] MACS2[91] was used for peak calling in Bedtools[90] sorted bam files. DeepTools[102] was used for peak merge, subtraction, and generating bigwig files for visualization. ChIPseeker was used for peak annotation and analyzing peak distribution.[93] For ATAC-Seq, motif enrichment analysis

was performed using HOMER,[103] and transcription factor footprints were analyzed via HINT-ATAC.[104]

QUANTIFICATION AND STATISTICAL ANALYSIS

Statistical analysis was performed using GraphPad Prism 9. Data were checked for normality using the Shapiro-Wilk test and for "normality vs. lognormality" when normalized to the control. Outliers were identified using ROUT with a Q value of 1% for raw data. To compare the difference between the two means, an unpaired Student's t-test was used. To compare means from more than two groups, one-way ANOVA, and for data with two independent variables, nonlinear regression or two-way ANOVA were used. To compare individual means, Sidak posthoc tests were used. For data that failed normality tests, we used the Mann-Whitney U test or Kruskal-Wallis test, followed by Dunn's comparisons as alternatives. All tests were performed with a two-tailed approach. Unless otherwise stated, continuous variables were presented as mean ± standard error of the mean (SEM). Results with $p < 0.05$ were considered statistically significant. All *in vitro* results with statistics represented at least three independent experiments.

Supplementary Material

Refer to Web version on PubMed Central for supplementary material.

ACKNOWLEDGMENTS

This study was partially supported by the National Institutes of Health grants HL153710 and HL138139 (J.Z.), HL109946 and HL134569 (Y.E.C.), HL151524 (L.C.), and HL150233 and DK134011 (O.R.); grants from the American Heart Association, 827942 (Y.Z.) and 936135 (G.Z.); and grant U2CDK110768 (Mouse Metabolic Phenotyping Center at Michigan). We used BioRender tools to adjust the graphic abstract. We extend our gratitude to Rose Ackermann from the University of Michigan for her assistance in establishing the FPLC assay

REFERENCES

1. Björkegren JLM, and Lusis AJ (2022). Atherosclerosis: Recent developments. Cell 185, 1630–1645. 10.1016/j.cell.2022.04.004. [PubMed: 35504280]
2. Libby P (2021). The biology of atherosclerosis comes full circle: lessons for conquering cardiovascular disease. Nat. Rev. Cardiol. 18, 683–684. 10.1038/s41569-021-00609-1. [PubMed: 34385684]
3. Banach M, and Penson PE (2021). Lipid-lowering therapies: Better together. Atherosclerosis 320, 86–88. 10.1016/j.atherosclerosis.2021.01.009. [PubMed: 33482997]
4. Vincent J (2018). Lipid Lowering Therapy for Atherosclerotic Cardiovascular Disease: It Is Not So Simple. Clin. Pharmacol. Ther. 104, 220–224. 10.1002/cpt.1138. [PubMed: 30117592]
5. Lorenzatti AJ (2021). Anti-inflammatory Treatment and Cardiovascular Outcomes: Results of Clinical Trials. Eur. Cardiol. 16, e15. 10.15420/ecr.2020.51. [PubMed: 33976710]
6. Brandes RP, and Gilsbach R (2021). Understanding Arteriosclerosis 2.0: Making Sense of Genetic Variants with scATAC. Circ. Res. 129, 259–261. 10.1161/CIRCRESAHA.121.319585. [PubMed: 34236882]
7. Örd T, Õunap K, Stolze LK, Aherrahrou R, Nurminen V, Toropainen A, Selvarajan I, Lönnberg T, Aavik E, Ylä-Herttuala S, et al. (2021). Single-Cell Epigenomics and Functional Fine-Mapping of Atherosclerosis GWAS Loci. Circ. Res. 129, 240–258. 10.1161/CIRCRESAHA.121.318971. [PubMed: 34024118]

8. Hou H, and Zhao H (2021). Epigenetic factors in atherosclerosis: DNA methylation, folic acid metabolism, and intestinal microbiota. Clin. Chim. Acta 512, 7–11. 10.1016/j.cca.2020.11.013. [PubMed: 33232735]
9. Zhang M, Zeng X, Yang Q, Xu J, Liu Z, Zhou Y, Cao Y, Zhang X, An X, Xu Y, et al. (2018). Ablation of Myeloid ADK (Adenosine Kinase) Epigenetically Suppresses Atherosclerosis in ApoE(−/−) (Apolipoprotein E Deficient) Mice. Arterioscl Throm Vas 38, 2780–2792. 10.1161/ATVBAHA.118.311806.
10. Chang Z, Zhao G, Zhao Y, Lu H, Xiong W, Liang W, Sun J, Wang H, Zhu T, Rom O, et al. (2020). BAF60a Deficiency in Vascular Smooth Muscle Cells Prevents Abdominal Aortic Aneurysm by Reducing Inflammation and Extracellular Matrix Degradation. Arterioscl Throm Vas 40, 2494–2507. 10.1161/ATVBAHA.120.314955.
11. Zhao G, Zhao Y, Lu H, Chang Z, Liu H, Wang H, Liang W, Liu Y, Zhu T, Rom O, et al. (2022). BAF60c prevents abdominal aortic aneurysm formation through epigenetic control of vascular smooth muscle cell homeostasis. J. Clin. Invest. 132, e158309. 10.1172/JCI158309. [PubMed: 36066968]
12. Lv YC, Tang YY, Zhang P, Wan W, Yao F, He PP, Xie W, Mo ZC, Shi JF, Wu JF, et al. (2016). Histone Methyltransferase Enhancer of Zeste Homolog 2-Mediated ABCA1 Promoter DNA Methylation Contributes to the Progression of Atherosclerosis. PLoS One 11, e0157265. 10.1371/journal.pone.0157265. [PubMed: 27295295]
13. Peng J, Yang Q, Li AF, Li RQ, Wang Z, Liu LS, Ren Z, Zheng XL, Tang XQ, Li GH, et al. (2016). Tet methylcytosine dioxygenase 2 inhibits atherosclerosis via upregulation of autophagy in ApoE−/− mice. Oncotarget 7, 76423–76436. 10.18632/oncotarget.13121. [PubMed: 27821816]
14. Liu Y, Zheng L, Wang Q, and Hu YW (2017). Emerging roles and mechanisms of long noncoding RNAs in atherosclerosis. Int. J. Cardiol. 228, 570–582. 10.1016/j.ijcard.2016.11.182. [PubMed: 27875736]
15. Ross R (1999). Atherosclerosis–an inflammatory disease. N. Engl. J. Med. 340, 115–126. 10.1056/NEJM199901143400207. [PubMed: 9887164]
16. Ait-Oufella H, Sage AP, Mallat Z, and Tedgui A (2014). Adaptive (T and B cells) immunity and control by dendritic cells in atherosclerosis. Circ. Res. 114, 1640–1660. 10.1161/CIRCRESAHA.114.302761. [PubMed: 24812352]
17. Liu Y, Zhao Y, Shukha Y, Lu H, Wang L, Liu Z, Liu C, Zhao Y, Wang H, Zhao G, et al. (2021). Dysregulated oxalate metabolism is a driver and therapeutic target in atherosclerosis. Cell Rep. 36, 109420. 10.1016/j.celrep.2021.109420. [PubMed: 34320345]
18. Jonasson L, Holm J, Skalli O, Bondjers G, and Hansson GK (1986). Regional accumulations of T cells, macrophages, and smooth muscle cells in the human atherosclerotic plaque. Arteriosclerosis 6, 131–138. 10.1161/01.atv.6.2.131. [PubMed: 2937395]
19. Doran AC, Lipinski MJ, Oldham SN, Garmey JC, Campbell KA, Skaflen MD, Cutchins A, Lee DJ, Glover DK, Kelly KA, et al. (2012). B-cell aortic homing and atheroprotection depend on Id3. Circ. Res. 110, e1–e12. 10.1161/CIRCRESAHA.111.256438. [PubMed: 22034493]
20. Zhou X, and Hansson GK (1999). Detection of B cells and proinflammatory cytokines in atherosclerotic plaques of hypercholesterolaemic apolipoprotein E knockout mice. Scand. J. Immunol. 50, 25–30. 10.1046/j.1365-3083.1999.00559.x. [PubMed: 10404048]
21. Gautier EL, Huby T, Saint-Charles F, Ouzilleau B, Pirault J, Deswaerte V, Ginhoux F, Miller ER, Witztum JL, Chapman MJ, and Lesnik P (2009). Conventional dendritic cells at the crossroads between immunity and cholesterol homeostasis in atherosclerosis. Circulation 119, 2367–2375. 10.1161/CIRCULATIONAHA.108.807537. [PubMed: 19380622]
22. Moroni F, Ammirati E, Norata GD, Magnoni M, and Camici PG (2019). The Role of Monocytes and Macrophages in Human Atherosclerosis, Plaque Neoangiogenesis, and Atherothrombosis. Mediators Inflamm. 2019, 7434376. 10.1155/2019/7434376. [PubMed: 31089324]
23. Reid MA, Dai Z, and Locasale JW (2017). The impact of cellular metabolism on chromatin dynamics and epigenetics. Nat. Cell Biol. 19, 1298–1306. 10.1038/ncb3629. [PubMed: 29058720]
24. Britt EC, John SV, Locasale JW, and Fan J (2020). Metabolic regulation of epigenetic remodeling in immune cells. Curr. Opin. Biotechnol. 63, 111–117. 10.1016/j.copbio.2019.12.008. [PubMed: 31954223]

25. Liu PS, Wang H, Li X, Chao T, Teav T, Christen S, Di Conza G, Cheng WC, Chou CH, Vavakova M, et al. (2017). alpha-ketoglutarate orchestrates macrophage activation through metabolic and epigenetic reprogramming. Nat. Immunol. 18, 985–994. 10.1038/ni.3796. [PubMed: 28714978]
26. Covarrubias AJ, Aksoylar HI, Yu J, Snyder NW, Worth AJ, Iyer SS, Wang J, Ben-Sahra I, Byles V, Polynne-Stapornkul T, et al. (2016). Akt-mTORC1 signaling regulates Acly to integrate metabolic input to control of macrophage activation. Elife 5, e11612. 10.7554/eLife.11612. [PubMed: 26894960]
27. Tong WH, Maio N, Zhang DL, Palmieri EM, Ollivierre H, Ghosh MC, McVicar DW, and Rouault TA (2018). TLR-activated repression of Fe-S cluster biogenesis drives a metabolic shift and alters histone and tubulin acetylation. Blood Adv. 2, 1146–1156. 10.1182/bloodadvances.2018015669. [PubMed: 29784770]
28. Langston PK, Nambu A, Jung J, Shibata M, Aksoylar HI, Lei J, Xu P, Doan MT, Jiang H, MacArthur MR, et al. (2019). Glycerol phosphate shuttle enzyme GPD2 regulates macrophage inflammatory responses. Nat. Immunol. 20, 1186–1195. 10.1038/s41590-019-0453-7. [PubMed: 31384058]
29. Seim GL, Britt EC, John SV, Yeo FJ, Johnson AR, Eisenstein RS, Pagliarini DJ, and Fan J (2019). Two-stage metabolic remodelling in macrophages in response to lipopolysaccharide and interferon-gamma stimulation. Nat. Metab. 1, 731–742. 10.1038/s42255-019-0083-2. [PubMed: 32259027]
30. Kwon H, Imbalzano AN, Khavari PA, Kingston RE, and Green MR (1994). Nucleosome disruption and enhancement of activator binding by a human SW1/SNF complex. Nature 370, 477–481. 10.1038/370477a0. [PubMed: 8047169]
31. Wang W, Côté J, Xue Y, Zhou S, Khavari PA, Biggar SR, Muchardt C, Kalpana GV, Goff SP, Yaniv M, et al. (1996). Purification and biochemical heterogeneity of the mammalian SWI-SNF complex. EMBO J. 15, 5370–5382. [PubMed: 8895581]
32. Centore RC, Sandoval GJ, Soares LMM, Kadoch C, and Chan HM (2020). Mammalian SWI/SNF Chromatin Remodeling Complexes: Emerging Mechanisms and Therapeutic Strategies. Trends Genet. 36, 936–950. 10.1016/j.tig.2020.07.011. [PubMed: 32873422]
33. Li S, Liu C, Li N, Hao T, Han T, Hill DE, Vidal M, and Lin JD (2008). Genome-wide coactivation analysis of PGC-1alpha identifies BAF60a as a regulator of hepatic lipid metabolism. Cell Metab. 8, 105–117. 10.1016/j.cmet.2008.06.013. [PubMed: 18680712]
34. Meng ZX, Wang L, Chang L, Sun J, Bao J, Li Y, Chen YE, and Lin JD (2015). A Diet-Sensitive BAF60a-Mediated Pathway Links Hepatic Bile Acid Metabolism to Cholesterol Absorption and Atherosclerosis. Cell Rep. 13, 1658–1669. 10.1016/j.celrep.2015.10.033. [PubMed: 26586440]
35. Liu T, Mi L, Xiong J, Orchard P, Yu Q, Yu L, Zhao XY, Meng ZX, Parker SCJ, Lin JD, and Li S (2020). BAF60a deficiency uncouples chromatin accessibility and cold sensitivity from white fat browning. Nat. Commun. 11, 2379. 10.1038/s41467-020-16148-1. [PubMed: 32404872]
36. Kong Q, Zou J, Zhang Z, Pan R, Zhang ZY, Han S, Xu Y, Gao Y, and Meng ZX (2022). BAF60a Deficiency in Macrophage Promotes Diet-Induced Obesity and Metabolic Inflammation. Diabetes 71, 2136–2152. 10.2337/db22-0114. [PubMed: 35822944]
37. Lin P, Ji HH, Li YJ, and Guo SD (2021). Macrophage Plasticity and Atherosclerosis Therapy. Front. Mol. Biosci. 8, 679797. 10.3389/fmolb.2021.679797. [PubMed: 34026849]
38. Zernecke A, Winkels H, Cochain C, Williams JW, Wolf D, Soehnlein O, Robbins CS, Monaco C, Park I, McNamara CA, et al. (2020). Meta-Analysis of Leukocyte Diversity in Atherosclerotic Mouse Aortas. Circ. Res. 127, 402–426. 10.1161/CIRCRESAHA.120.316903. [PubMed: 32673538]
39. Hu W, Lu H, Zhang J, Fan Y, Chang Z, Liang W, Wang H, Zhu T, Garcia-Barrio MT, Peng D, et al. (2018). Kruppel-like factor 14, a coronary artery disease associated transcription factor, inhibits endothelial inflammation via NF-kappaB signaling pathway. Atherosclerosis 278, 39–48. 10.1016/j.atherosclerosis.2018.09.018. [PubMed: 30248551]
40. Duroux-Richard I, Apparailly F, and Khoury M (2021). Mitochondrial MicroRNAs Contribute to Macrophage Immune Functions Including Differentiation, Polarization, and Activation. Front. Physiol. 12, 738140. 10.3389/fphys.2021.738140. [PubMed: 34803730]

41. Qing J, Zhang Z, Nová k P, Zhao G, and Yin K (2020). Mitochondrial metabolism in regulating macrophage polarization: an emerging regulator of metabolic inflammatory diseases. Acta Biochim. Biophys. Sin. 52, 917–926. 10.1093/abbs/gmaa081. [PubMed: 32785581]
42. Orekhov AN, Poznyak AV, Sobenin IA, Nikifirov NN, and Ivanova EA (2020). Mitochondrion as a Selective Target for the Treatment of Atherosclerosis: Role of Mitochondrial DNA Mutations and Defective Mitophagy in the Pathogenesis of Atherosclerosis and Chronic Inflammation. Curr. Neuropharmacol. 18, 1064–1075. 10.2174/1570159X17666191118125018. [PubMed: 31744449]
43. Feng J, Li L, Ou Z, Li Q, Gong B, Zhao Z, Qi W, Zhou T, Zhong J, Cai W, et al. (2018). IL-25 stimulates M2 macrophage polarization and thereby promotes mitochondrial respiratory capacity and lipolysis in adipose tissues against obesity. Cell. Mol. Immunol. 15, 493–505. 10.1038/cmi.2016.71. [PubMed: 28194019]
44. Van den Bossche J, Baardman J, Otto NA, van der Velden S, Neele AE, van den Berg SM, Luque-Martin R, Chen HJ, Boshuizen MCS, Ahmed M, et al. (2016). Mitochondrial Dysfunction Prevents Repolarization of Inflammatory Macrophages. Cell Rep. 17, 684–696. 10.1016/j.celrep.2016.09.008. [PubMed: 27732846]
45. Van den Bossche J, Baardman J, and de Winther MP (2015). Metabolic Characterization of Polarized M1 and M2 Bone Marrow-derived Macrophages Using Real-time Extracellular Flux Analysis. J. Vis. Exp. 10.3791/53424.
46. Zhang S, Liu Y, Cao Y, Zhang S, Sun J, Wang Y, Song S, and Zhang H (2022). Targeting the Microenvironment of Vulnerable Atherosclerotic Plaques: An Emerging Diagnosis and Therapy Strategy for Atherosclerosis. Adv. Mater. 34, e2110660. 10.1002/adma.202110660. [PubMed: 35238081]
47. Ward LJ, Ljunggren SA, Karlsson H, Li W, and Yuan XM (2017). Exposure to atheroma-relevant 7-oxysterols causes proteomic alterations in cell death, cellular longevity, and lipid metabolism in THP-1 macrophages. PLoS One 12, e0174475. 10.1371/journal.pone.0174475. [PubMed: 28350877]
48. Xiao Q, Che X, Cai B, Tao Z, Zhang H, Shao Q, and Pu J (2020). Macrophage autophagy regulates mitochondria-mediated apoptosis and inhibits necrotic core formation in vulnerable plaques. J. Cell Mol. Med. 24, 260–275. 10.1111/jcmm.14715. [PubMed: 31660692]
49. Shioi A, and Ikari Y (2018). Plaque Calcification During Atherosclerosis Progression and Regression. J. Atheroscler. Thromb. 25, 294–303. 10.5551/jat.RV17020. [PubMed: 29238011]
50. Jinnouchi H, Guo L, Sakamoto A, Torii S, Sato Y, Cornelissen A, Kuntz S, Paek KH, Fernandez R, Fuller D, et al. (2020). Diversity of macrophage phenotypes and responses in atherosclerosis. Cell. Mol. Life Sci. 77, 1919–1932. 10.1007/s00018-019-03371-3. [PubMed: 31720740]
51. Boyle JJ, Johns M, Lo J, Chiodini A, Ambrose N, Evans PC, Mason JC, and Haskard DO (2011). Heme induces heme oxygenase 1 via Nrf2: role in the homeostatic macrophage response to intraplaque hemorrhage. Arterioscl Throm Vas 31, 2685–2691. 10.1161/ATVBAHA.111.225813.
52. Chinetti-Gbaguidi G, Baron M, Bouhlel MA, Vanhoutte J, Copin C, Sebti Y, Derudas B, Mayi T, Bories G, Tailleux A, et al. (2011). Human atherosclerotic plaque alternative macrophages display low cholesterol handling but high phagocytosis because of distinct activities of the PPARgamma and LXRalpha pathways. Circ. Res. 108, 985–995. 10.1161/CIRCRESAHA.110.233775. [PubMed: 21350215]
53. Li Y, Cai L, Wang H, Wu P, Gu W, Chen Y, Hao H, Tang K, Yi P, Liu M, et al. (2011). Pleiotropic regulation of macrophage polarization and tumorigenesis by formyl peptide receptor-2. Oncogene 30, 3887–3899. 10.1038/onc.2011.112. [PubMed: 21499310]
54. Colin S, Chinetti-Gbaguidi G, and Staels B (2014). Macrophage phenotypes in atherosclerosis. Immunol. Rev. 262, 153–166. 10.1111/imr.12218. [PubMed: 25319333]
55. Domschke G, and Gleissner CA (2019). CXCL4-induced macrophages in human atherosclerosis. Cytokine 122, 154141. 10.1016/j.cyto.2017.08.021. [PubMed: 28899579]
56. Kadl A, Meher AK, Sharma PR, Lee MY, Doran AC, Johnstone SR, Elliott MR, Gruber F, Han J, Chen W, et al. (2010). Identification of a novel macrophage phenotype that develops in response to atherogenic phospholipids via Nrf2. Circ. Res. 107, 737–746. 10.1161/CIRCRESAHA.109.215715. [PubMed: 20651288]

57. Cochain C, Vafadarnejad E, Arampatzi P, Pelisek J, Winkels H, Ley K, Wolf D, Saliba AE, and Zernecke A (2018). Single-Cell RNA-Seq Reveals the Transcriptional Landscape and Heterogeneity of Aortic Macrophages in Murine Atherosclerosis. Circ. Res. 122, 1661–1674. 10.1161/CIRCRESAHA.117.312509. [PubMed: 29545365]
58. Zhao G, Lu H, Chang Z, Zhao Y, Zhu T, Chang L, Guo Y, Garcia-Barrio MT, Chen YE, and Zhang J (2021). Single-cell RNA sequencing reveals the cellular heterogeneity of aneurysmal infrarenal abdominal aorta. Cardiovasc. Res. 117, 1402–1416. 10.1093/cvr/cvaa214. [PubMed: 32678909]
59. Zhao G, Lu H, Liu Y, Zhao Y, Zhu T, Garcia-Barrio MT, Chen YE, and Zhang J (2021). Single-Cell Transcriptomics Reveals Endothelial Plasticity During Diabetic Atherogenesis. Front. Cell Dev. Biol. 9, 689469. 10.3389/fcell.2021.689469. [PubMed: 34095155]
60. Kim K, Shim D, Lee JS, Zaitsev K, Williams JW, Kim KW, Jang MY, Seok Jang H, Yun TJ, Lee SH, et al. (2018). Transcriptome Analysis Reveals Nonfoamy Rather Than Foamy Plaque Macrophages Are Proinflammatory in Atherosclerotic Murine Models. Circ. Res. 123, 1127–1142. 10.1161/CIRCRESAHA.118.312804. [PubMed: 30359200]
61. Lin JD, Nishi H, Poles J, Niu X, McCauley C, Rahman K, Brown EJ, Yeung ST, Vozhilla N, Weinstock A, et al. (2019). Single-cell analysis of fate-mapped macrophages reveals heterogeneity, including stem-like properties, during atherosclerosis progression and regression. JCI Insight 4, e124574. 10.1172/jci.insight.124574. [PubMed: 30830865]
62. Xiong X, Kuang H, Ansari S, Liu T, Gong J, Wang S, Zhao XY, Ji Y, Li C, Guo L, et al. (2019). Landscape of Intercellular Crosstalk in Healthy and NASH Liver Revealed by Single-Cell Secretome Gene Analysis. Mol. Cell 75, 644–660.e5. 10.1016/j.molcel.2019.07.028. [PubMed: 31398325]
63. Alsaigh T, Evans D, Frankel D, and Torkamani A (2022). Decoding the transcriptome of calcified atherosclerotic plaque at single-cell resolution. Commun. Biol. 5, 1084. 10.1038/s42003-022-04056-7. [PubMed: 36224302]
64. Hao Y, Hao S, Andersen-Nissen E, Mauck WM 3rd, Zheng S, Butler A, Lee MJ, Wilk AJ, Darby C, Zager M, et al. (2021). Integrated analysis of multimodal single-cell data. Cell 184, 3573–3587.e29. 10.1016/j.cell.2021.04.048. [PubMed: 34062119]
65. Newman AM, Steen CB, Liu CL, Gentles AJ, Chaudhuri AA, Scherer F, Khodadoust MS, Esfahani MS, Luca BA, Steiner D, et al. (2019). Determining cell type abundance and expression from bulk tissues with digital cytometry. Nat. Biotechnol. 37, 773–782. 10.1038/s41587-019-0114-2. [PubMed: 31061481]
66. Lissanu Deribe Y, Sun Y, Terranova C, Khan F, Martinez-Ledesma J, Gay J, Gao G, Mullinax RA, Khor T, Feng N, et al. (2018). Mutations in the SWI/SNF complex induce a targetable dependence on oxidative phosphorylation in lung cancer. Nat. Med. 24, 1047–1057. 10.1038/s41591-018-0019-5. [PubMed: 29892061]
67. Shi Y, Zhang H, Huang S, Yin L, Wang F, Luo P, and Huang H (2022). Epigenetic regulation in cardiovascular disease: mechanisms and advances in clinical trials. Signal Transduct. Target. Ther. 7, 200. 10.1038/s41392-022-01055-2. [PubMed: 35752619]
68. Bartholomew B (2014). Regulating the chromatin landscape: structural and mechanistic perspectives. Annu. Rev. Biochem. 83, 671–696. 10.1146/annurev-biochem-051810-093157. [PubMed: 24606138]
69. Stankunas K, Hang CT, Tsun ZY, Chen H, Lee NV, Wu JI, Shang C, Bayle JH, Shou W, Iruela-Arispe ML, and Chang CP (2008). Endocardial Brg1 represses ADAMTS1 to maintain the microenvironment for myocardial morphogenesis. Dev. Cell 14, 298–311. 10.1016/j.devcel.2007.11.018. [PubMed: 18267097]
70. Ramirez-Carrozzi VR, Nazarian AA, Li CC, Gore SL, Sridharan R, Imbalzano AN, and Smale ST (2006). Selective and antagonistic functions of SWI/SNF and Mi-2beta nucleosome remodeling complexes during an inflammatory response. Genes Dev. 20, 282–296. 10.1101/gad.1383206. [PubMed: 16452502]
71. Gatchalian J, Liao J, Maxwell MB, and Hargreaves DC (2020). Control of Stimulus-Dependent Responses in Macrophages by SWI/SNF Chromatin Remodeling Complexes. Trends Immunol. 41, 126–140. 10.1016/j.it.2019.12.002. [PubMed: 31928914]
72. Hsiao PW, Fryer CJ, Trotter KW, Wang W, and Archer TK (2003). BAF60a mediates critical interactions between nuclear receptors and the BRG1 chromatin-remodeling complex for

transactivation. Mol. Cell Biol. 23, 6210–6220. 10.1128/MCB.23.17.6210-6220.2003. [PubMed: 12917342]

73. Lee YS, Sohn DH, Han D, Lee HW, Seong RH, and Kim JB (2007). Chromatin remodeling complex interacts with ADD1/SREBP1c to mediate insulin-dependent regulation of gene expression. Mol. Cell Biol. 27, 438–452. 10.1128/MCB.00490-06. [PubMed: 17074803]
74. Shrivastava R, Asif M, Singh V, Dubey P, Ahmad Malik S, Lone MUD, Tewari BN, Baghel KS, Pal S, Nagar GK, et al. (2019). M2 polarization of macrophages by Oncostatin M in hypoxic tumor microenvironment is mediated by mTORC2 and promotes tumor growth and metastasis. Cytokine 118, 130–143. 10.1016/j.cyto.2018.03.032. [PubMed: 29625858]
75. Gordon S, and Martinez FO (2010). Alternative activation of macrophages: mechanism and functions. Immunity 32, 593–604. 10.1016/j.immuni.2010.05.007. [PubMed: 20510870]
76. Cabrera JA, Ziemba EA, Colbert R, Kelly RF, Kuskowski M, Arriaga EA, Sluiter W, Duncker DJ, Ward HB, and McFalls EO (2012). Uncoupling protein-2 expression and effects on mitochondrial membrane potential and oxidant stress in heart tissue. Transl. Res. 159, 383–390. 10.1016/j.trsl.2011.11.001. [PubMed: 22500511]
77. O'Neill LAJ, and Pearce EJ (2016). Immunometabolism governs dendritic cell and macrophage function. J. Exp. Med. 213, 15–23. 10.1084/jem.20151570. [PubMed: 26694970]
78. Tomas L, Edsfeldt A, Mollet IG, Perisic Matic L, Prehn C, Adamski J, Paulsson-Berne G, Hedin U, Nilsson J, Bengtsson E, et al. (2018). Altered metabolism distinguishes high-risk from stable carotid atherosclerotic plaques. Eur. Heart J. 39, 2301–2310. 10.1093/eurheartj/ehy124. [PubMed: 29562241]
79. Madamanchi NR, and Runge MS (2007). Mitochondrial dysfunction in atherosclerosis. Circ. Res. 100, 460–473. 10.1161/01.RES.0000258450.44413.96. [PubMed: 17332437]
80. Martinet W, Coornaert I, Puylaert P, and De Meyer GRY (2019). Macrophage Death as a Pharmacological Target in Atherosclerosis. Front. Pharmacol. 10, 306. 10.3389/fphar.2019.00306. [PubMed: 31019462]
81. Mantovani A, Sica A, Sozzani S, Allavena P, Vecchi A, and Locati M (2004). The chemokine system in diverse forms of macrophage activation and polarization. Trends Immunol. 25, 677–686. 10.1016/j.it.2004.09.015. [PubMed: 15530839]
82. Davies LC, Jenkins SJ, Allen JE, and Taylor PR (2013). Tissue-resident macrophages. Nat. Immunol. 14, 986–995. 10.1038/ni.2705. [PubMed: 24048120]
83. Scarpulla RC (2008). Transcriptional paradigms in mammalian mitochondrial biogenesis and function. Physiol. Rev. 88, 611–638. 10.1152/physrev.00025.2007. [PubMed: 18391175]
84. Chong H, Wei Z, Na M, Sun G, Zheng S, Zhu X, Xue Y, Zhou Q, Guo S, Xu J, et al. (2020). The PGC-1alpha/NRF1/miR-378a axis protects vascular smooth muscle cells from FFA-induced proliferation, migration and inflammation in atherosclerosis. Atherosclerosis 297, 136–145. 10.1016/j.atherosclerosis.2020.02.001. [PubMed: 32120345]
85. Karunakaran D, Thrush AB, Nguyen MA, Richards L, Geoffrion M, Singaravelu R, Ramphos E, Shangari P, Ouimet M, Pezacki JP, et al. (2015). Macrophage Mitochondrial Energy Status Regulates Cholesterol Efflux and Is Enhanced by Anti-miR33 in Atherosclerosis. Circ. Res. 117, 266–278. 10.1161/Circresaha.117.305624. [PubMed: 26002865]
86. Huang JY, Chiou HY, Lien LM, Jeng JS, Lin HJ, Hu CJ, and Hsieh FI (2019). Significant Associations Of Nrf1 Genetic Polymorphisms With The Risk Of Early-Onset Ischemic Stroke. Atherosclerosis 287, e162–e163. 10.1016/j.atherosclerosis.2019.06.490.
87. Baitsch D, Telgmann R, Varga G, Muller-Tidow C, Bot M, and Nofer JR (2008). Apolipoprotein E (ApoE) Induces an Anti-inflammatory Phenotype in Macrophages. Circulation 118, S377.
88. Langmead B, and Salzberg SL (2012). Fast gapped-read alignment with Bowtie 2. Nat. Methods 9, 357–359. 10.1038/nmeth.1923. [PubMed: 22388286]
89. Danecek P, Bonfield JK, Liddle J, Marshall J, Ohan V, Pollard MO, Whitwham A, Keane T, McCarthy SA, Davies RM, and Li H (2021). Twelve years of SAMtools and BCFtools. GigaScience 10, giab008. 10.1093/gigascience/giab008. [PubMed: 33590861]
90. Quinlan AR, and Hall IM (2010). BEDTools: a flexible suite of utilities for comparing genomic features. Bioinformatics 26, 841–842. 10.1093/bioinformatics/btq033. [PubMed: 20110278]

91. Zhang Y, Liu T, Meyer CA, Eeckhoute J, Johnson DS, Bernstein BE, Nusbaum C, Myers RM, Brown M, Li W, and Liu XS (2008). Model-based analysis of ChIP-Seq (MACS). Genome Biol. 9, R137. 10.1186/gb-2008-9-9-r137. [PubMed: 18798982]
92. Ewels P, Magnusson M, Lundin S, and Käller M (2016). MultiQC: summarize analysis results for multiple tools and samples in a single report. Bioinformatics 32, 3047–3048. 10.1093/bioinformatics/btw354. [PubMed: 27312411]
93. Yu G, Wang LG, and He QY (2015). ChIPseeker: an R/Bioconductor package for ChIP peak annotation, comparison and visualization. Bioinformatics 31, 2382–2383. 10.1093/bioinformatics/btv145. [PubMed: 25765347]
94. Love MI, Huber W, and Anders S (2014). Moderated estimation of fold change and dispersion for RNA-seq data with DESeq2. Genome Biol. 15, 550. 10.1186/s13059-014-0550-8. [PubMed: 25516281]
95. Wu T, Hu E, Xu S, Chen M, Guo P, Dai Z, Feng T, Zhou L, Tang W, Zhan L, et al. (2021). clusterProfiler 4.0: A universal enrichment tool for interpreting omics data. Innovation 2, 100141. 10.1016/j.xinn.2021.100141. [PubMed: 34557778]
96. Mas G, Man N, Nakata Y, Martinez-Caja C, Karl D, Beckedorff F, Tamiro F, Chen C, Duffort S, Itonaga H, et al. (2023). The SWI/SNF chromatin-remodeling subunit DPF2 facilitates NRF2-dependent anti-inflammatory and antioxidant gene expression. J. Clin. Invest. 133, e158419. 10.1172/JCI158419. [PubMed: 37200093]
97. ENCODE Project Consortium (2012). An integrated encyclopedia of DNA elements in the human genome. Nature 489, 57–74. 10.1038/nature11247. [PubMed: 22955616]
98. Zhu W, Liang W, Lu H, Chang L, Zhang J, Chen YE, and Guo Y (2022). Myeloid TM6SF2 Deficiency Inhibits Atherosclerosis. Cells 11. 10.3390/cells11182877. [PubMed: 36611806]
99. Nascimbeni F, Bedossa P, Fedchuk L, Pais R, Charlotte F, Lebray P, Poynard T, and Ratziu V; LIDO Liver Injury in Diabetes and Obesity Study Group (2020). Clinical validation of the FLIP algorithm and the SAF score in patients with non-alcoholic fatty liver disease. J. Hepatol. 72, 828–838. 10.1016/j.jhep.2019.12.008. [PubMed: 31862486]
100. Zhao Y, Chang Z, Zhao G, Lu H, Xiong W, Liang W, Wang H, Villacorta L, Garcia-Barrio MT, Zhu T, et al. (2021). Suppression of Vascular Macrophage Activation by Nitro-Oleic Acid and its Implication for Abdominal Aortic Aneurysm Therapy. Cardiovasc. Drugs Ther. 35, 939–951. 10.1007/s10557-020-07031-8. [PubMed: 32671602]
101. Lu H, Fan Y, Qiao C, Liang W, Hu W, Zhu T, Zhang J, and Chen YE (2017). TFEB inhibits endothelial cell inflammation and reduces atherosclerosis. Sci. Signal. 10, eaah4214. 10.1126/scisignal.aah4214. [PubMed: 28143903]
102. Ramírez F, Ryan DP, Grüning B, Bhardwaj V, Kilpert F, Richter AS, Heyne S, Dündar F, and Manke T (2016). deepTools2: a next generation web server for deep-sequencing data analysis. Nucleic Acids Res. 44, W160–W165. 10.1093/nar/gkw257. [PubMed: 27079975]
103. Heinz S, Benner C, Spann N, Bertolino E, Lin YC, Laslo P, Cheng JX, Murre C, Singh H, and Glass CK (2010). Simple combinations of lineage-determining transcription factors prime cis-regulatory elements required for macrophage and B cell identities. Mol. Cell 38, 576–589. 10.1016/j.molcel.2010.05.004. [PubMed: 20513432]
104. Li Z, Schulz MH, Look T, Begemann M, Zenke M, and Costa IG (2019). Identification of transcription factor binding sites using ATAC-seq. Genome Biol. 20, 45. 10.1186/s13059-019-1642-2. [PubMed: 30808370]

Highlights

- *Baf60a* downregulation in macrophages exacerbates atherosclerosis
- *Baf60a* deficiency affects macrophage mitochondrial homeostasis
- NRF1 transcriptional response to stress is altered by *Baf60a* deficiency
- BAF60a-NRF1 interaction counters mitochondrial impairment under atherosclerosis

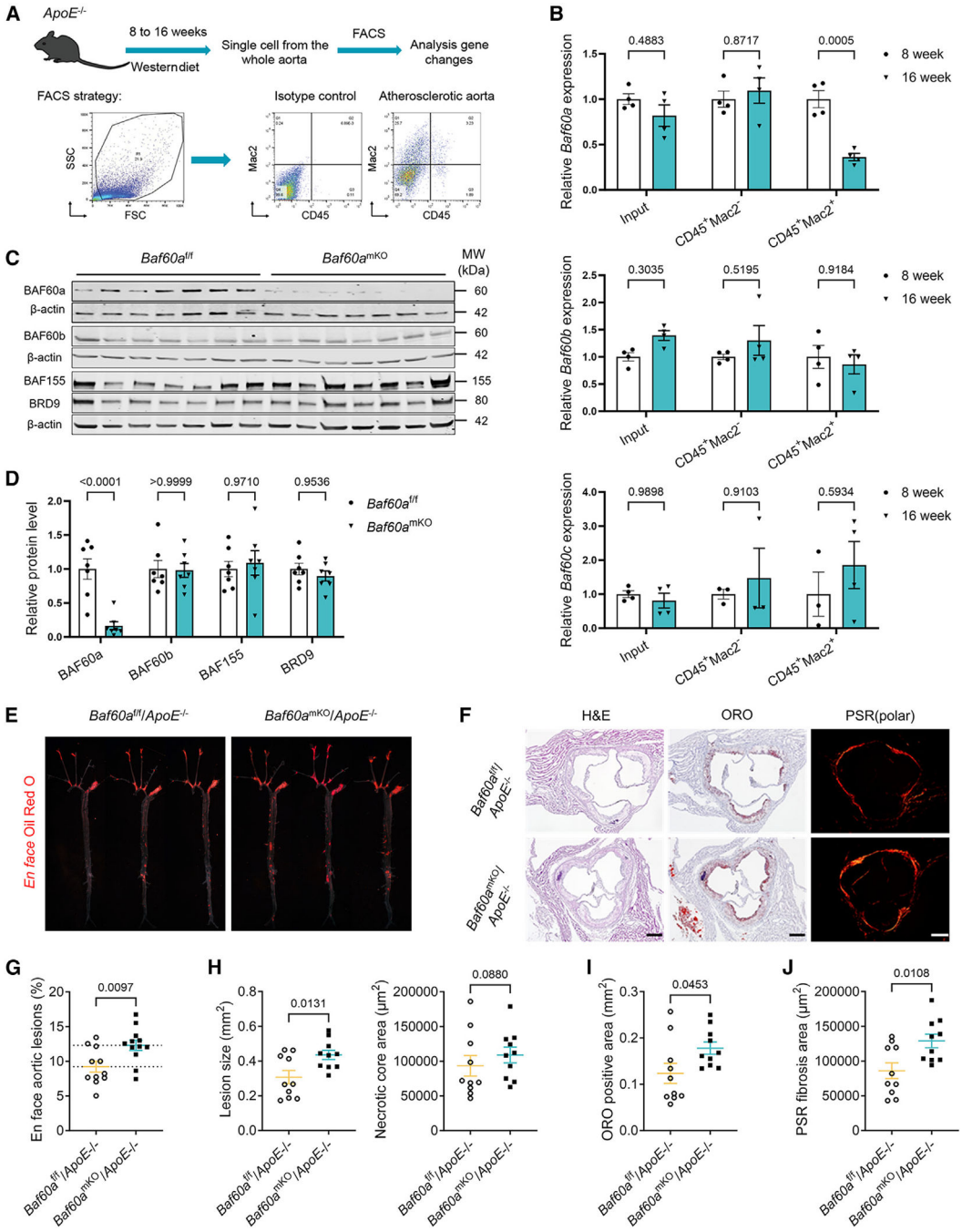

Figure 1. Downregulation of *Baf60a* in advanced atherosclerotic plaque macrophages exacerbates atherosclerosis in *ApoE*$^{-/-}$ hypercholesterolemic mice

(A) FACS isolation of single aortic cells from atherosclerotic *ApoE*$^{-/-}$ mice at 8 or 16 weeks post WD feeding.

(B) qPCR measurement of mRNA abundance for *Baf60a*, *Baf60b*, and *Baf60c*. Each data point represents pooled samples from three mice (n = 4).

(C and D) (C) Immunoblotting and (D) quantification of BAF60a, BAF60b, BAF155, BRD9, and β-actin protein abundance in BMDMs isolated from *Baf60a*^{mKO} and *Baf60a*$^{f/f}$ mice (n = 7; membranes were reused in Figure S4A).

(E–J) Male *Baf60a*$^{f/f}$/*ApoE*$^{-/-}$ and *Baf60a*^{mKO}/*ApoE*$^{-/-}$ mice were fed a WD for 16 weeks (n = 13–15 per group). (E) En-face ORO staining of the aortic tree. (F) H&E, ORO, and PSR staining of the aortic root. Scale bars, 200 μm. (G) Quantification of en-face ORO staining of the aortic tree. (H) H&E staining of the aortic root followed by quantification of lesion and necrotic core area. (I) Quantification of ORO-positive aortic root area. (J) Quantification of PSR-positive fibrotic region in the aortic root.

Data are presented as mean ± SEM. Two-way ANOVA followed by Holm-Sidak multiple comparisons for (B) and (D); Student's t test for (G)–(J).

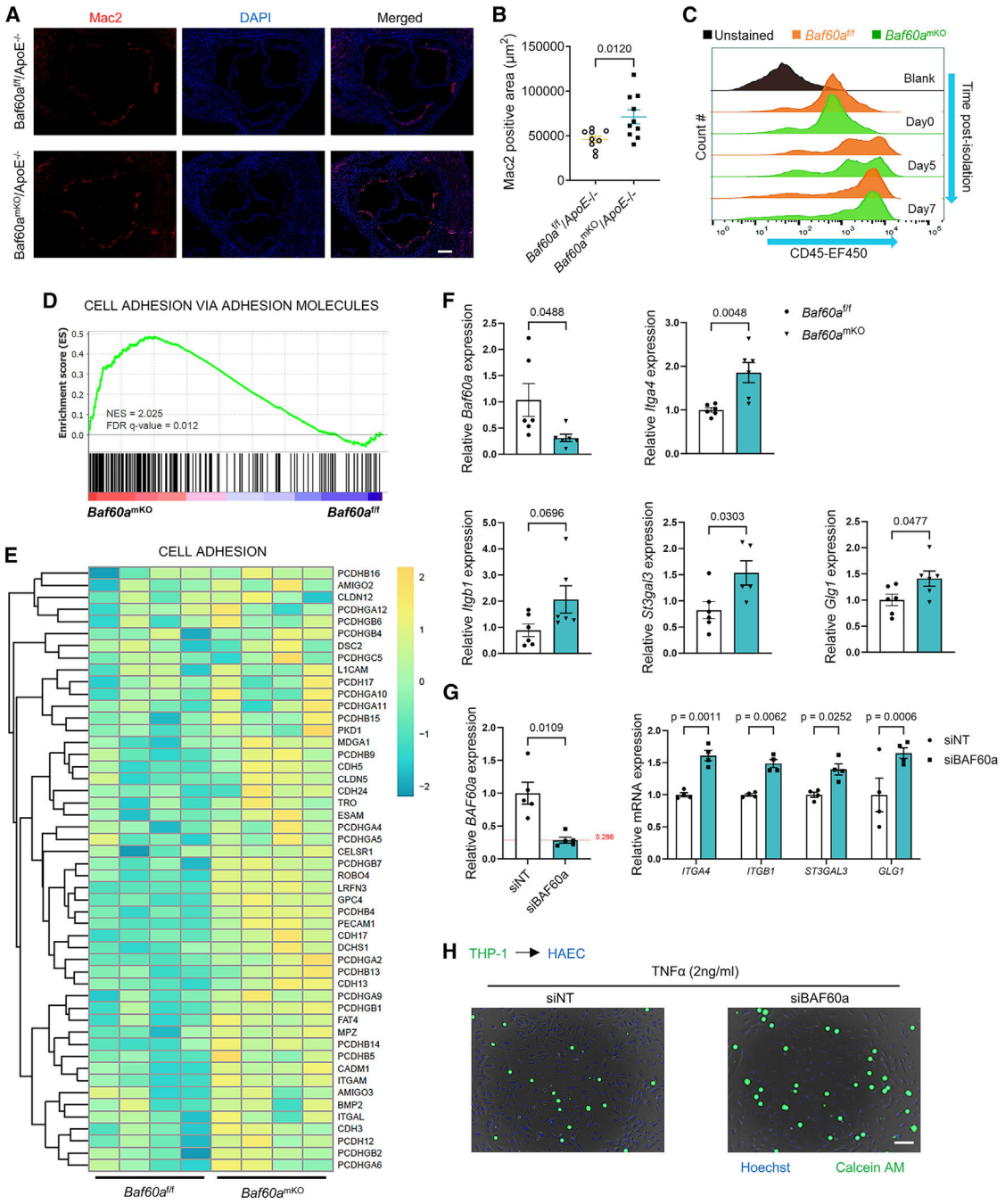

Figure 2. Myeloid *Baf60a* deletion induces vascular immune cell recruitment

Male *Baf60a*^{mKO}/*ApoE*$^{-/-}$ and *Baf60a*$^{f/f}$/*ApoE*$^{-/-}$ mice were fed a WD for 16 weeks.

(A and B) Immunofluorescence staining at the aortic root region demonstrating Mac2-positive macrophage and immune cell content, followed by quantification (B).

(C) FACS histogram of dynamic changes in CD45 expression during 7 days of BMDM differentiation.

(D) RNA-seq of BMDM from *Baf60a*^{mKO} and *Baf60a*$^{f/f}$ mice (n = 4) followed by GSEA.

(E) Heatmap of adhesion-related gene expression from (D).

(F) qPCR of the adhesion-related genes in CD11b-positive PBMCs from *Baf60a*^{mKO} or *Baf60a*$^{f/f}$ mice (n = 6).

(G) qPCR of the adhesion-related genes from THP-1 cells transfected with siNT or siBAF60a at 72 h post transfection (n = 4).

(H) Representative figures of Calcein AM-stained THP-1 cell attached to TNF-α-activated HAECs. Scale bar, 100 μm.

Data are presented as mean ± SEM. Student's t test for (B), (F), and (G) (left); two-way ANOVA followed by Holm-Sidak post hoc analysis for (G) (right).

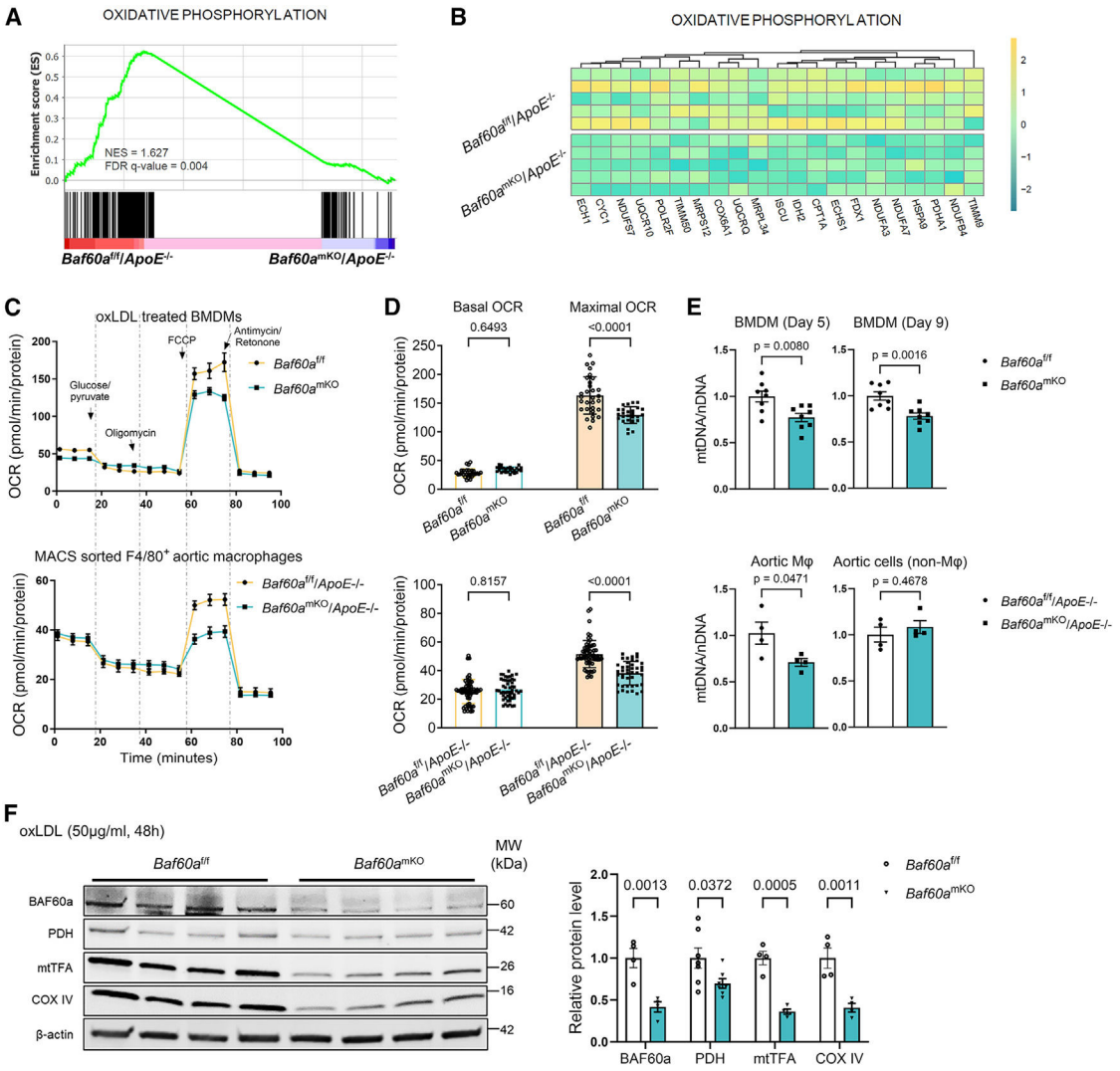

Figure 3. Mitochondrial content decreased in *Baf60a*-deficient atherosclerotic macrophages

(A) RNA-seq of BMDMs isolated from 16-week WD feeding atherosclerotic *Baf60a*^{mKO}/*ApoE*$^{-/-}$ and *Baf60a*$^{f/f}$/*ApoE*$^{-/-}$ mice followed by GSEA.

(B) Heatmap of OXPHOS-related gene expression from (A).

(C) Upper: Seahorse measurement of OCR in *Baf60a*^{mKO} and *Baf60a*$^{f/f}$ BMDMs treated with oxLDL (50 μg/mL, 48 h, n = 26–30 per group). Lower: Seahorse measurement of OCR in F4/80^{+} aortic macrophage from 16-week WD-fed *Baf60a*^{mKO}/*ApoE*$^{-/-}$ and *Baf60a*$^{f/f}$/*ApoE*$^{-/-}$ mice (n = 42–60 per group).

(D) Quantification of basal and maximal OCR.

(E) Upper: qPCR quantification of mtDNA/nDNA ratio in *Baf60a*^{mKO} and *Baf60a*$^{f/f}$ bone marrow-derived monocytes or macrophages treated with oxLDL(50 μg/mL, 48 h, n = 8). Lower: qPCR quantification of mtDNA/nDNA ratio in FACS-sorted F4/80^{+} aortic macrophages and non-macrophages from 16-week WD-fed *Baf60a*^{mKO}/*ApoE*$^{-/-}$ and *Baf60a*$^{f/f}$/*ApoE*$^{-/-}$ mice (n = 8 per group).

(F) Immunoblotting and quantification of BAF60a, PDH, mtTFA, COX IV, and β-actin protein abundance in BMDMs from *Baf60a*^{mKO} or *Baf60a*$^{f/f}$ mice treated with oxLDL (50 μg/mL, 48 h, n = 4–7 per group).

Data are presented as mean ± SEM. Two-way ANOVA followed by Holm-Sidak post hoc analysis for (D) and (F); Student's t test for (E).

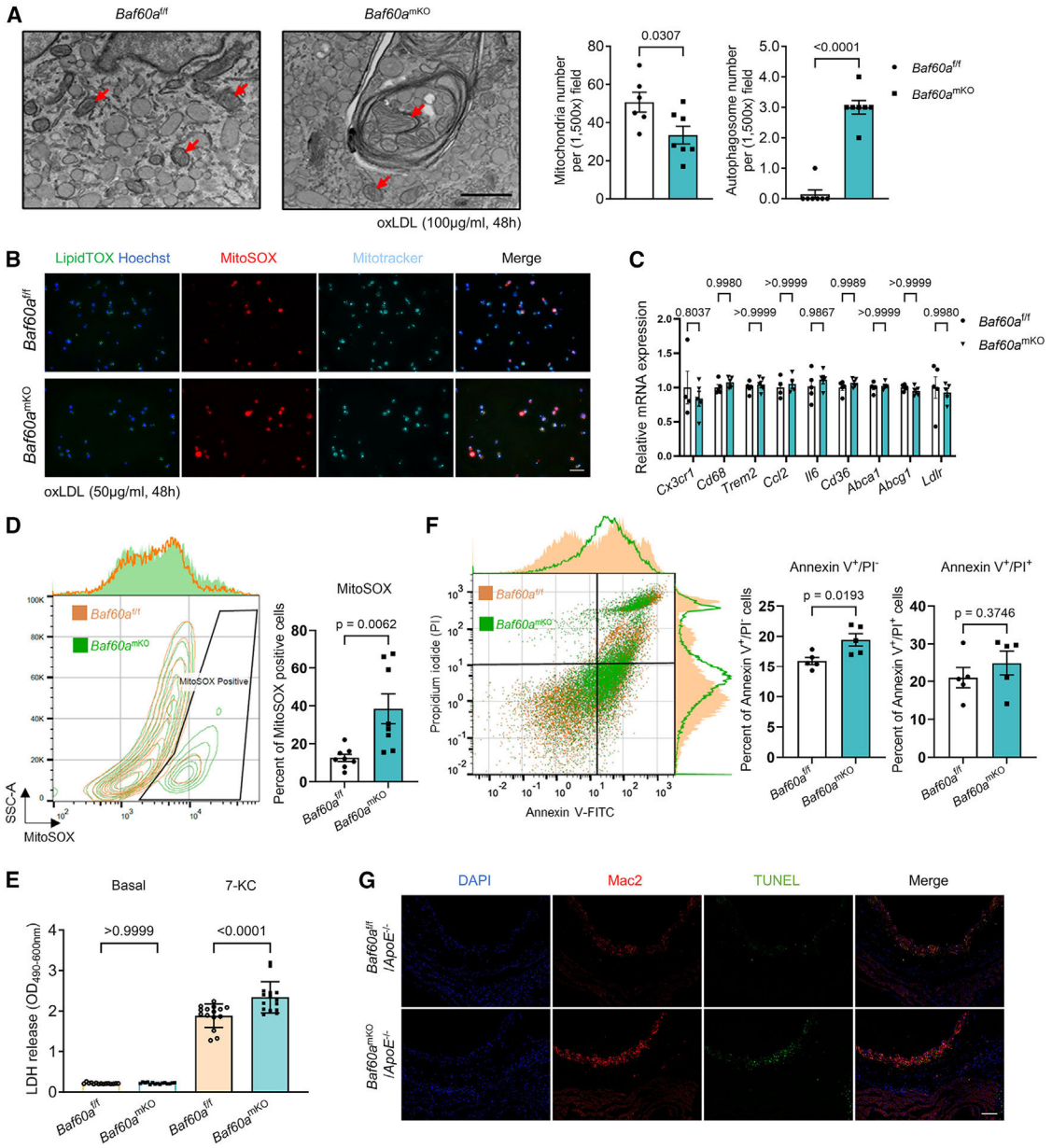

Figure 4. Atherosclerotic environmental cues link *Baf60a* deficiency to mitochondria dysfunction, ROS generation, and apoptosis

(A) TEM imaging of BMDMs from *Baf60a*^{mKO} or *Baf60a*$^{f/f}$ mice treated with oxLDL (100 mg/mL, 48 h), followed by quantification of individual mitochondrion and autophagosome numbers (n = 6–7 per group). Scale bar, 800 nm.

(B) Hoechst, LipidTOX, MitoSOX, and MitoTracker staining of BMDMs isolated from *Baf60a*^{mKO} or *Baf60a*$^{f/f}$ mice and treated with oxLDL (50 μg/mL, 48 h). Scale bar, 100 μm.

(C) qPCR quantification of mRNA extracted from *Baf60a*^{mKO} or *Baf60a*$^{f/f}$ BMDMs and treated with oxLDL (50 μg/mL for 48 h, n = 4–5 per group).

(D) Density plot and FACS analysis of BMDMs from *Baf60a*^{mKO} or *Baf60a*$^{f/f}$ mice treated with oxLDL (50 μg/mL, 48 h) and stained with MitoSOX (n = 8).

(E) LDH release from vehicle control or 7-KC (10 μg/mL, 24 h)-treated BMDMs isolated from either *Baf60a*^{mKO} or *Baf60a*$^{f/f}$ mice (n = 15).

(F) Dot plot and FACS analysis of BMDMs from *Baf60a*^{mKO} or *Baf60a*$^{f/f}$ mice treated with 7-KC (10 μg/mL, 24 h) and stained with annexin V/PI to quantify apoptotic cell number (n = 5).

(G) Immunofluorescence illustration of aortic sinus from 16-week WD-fed *Baf60a*^{mKO}/*ApoE*$^{-/-}$ and *Baf60a*$^{f/f}$/*ApoE*$^{-/-}$ mice co-stained with DAPI, Mac2, and TUNEL. Scale bar, 50 μm.

Data are presented as mean ± SEM. Student's t test for (A) and (D)–(F); two-way ANOVA followed by Holm-Sidak post hoc analysis for (C) and (E).

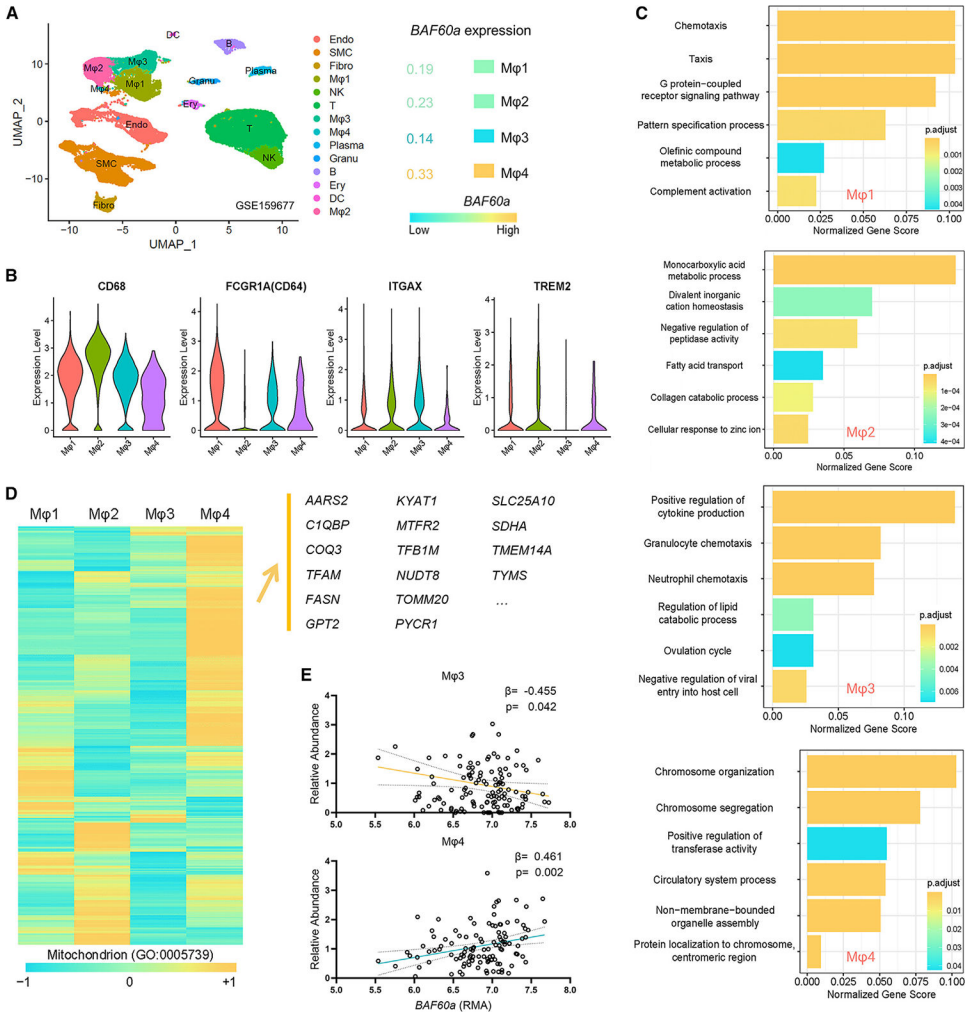

Figure 5. Correlation between *BAF60a* expression and mitochondrial gene expression in plaque macrophages from human patients

(A) UMAP (uniform manifold approximation and projection) plot of different cell types defined by human plaque scRNA-seq (GEO: GSE159677) and corresponding cluster-wise *BAF60a* expression.

(B) Violin plot of common macrophage marker expression in Mφ1 to Mφ4 clusters.

(C) Gene ontology (GO) enrichment analysis of gene expression in Mφ1 to Mφ4 clusters.

(D) Heatmap of normalized mitochondria-related gene expression in Mφ1 to Mφ4 clusters.

(E) Bulk plaque sequencing deconvolution using a curated single-cell signature matrix, followed by Pearson correlation analysis (n = 126).

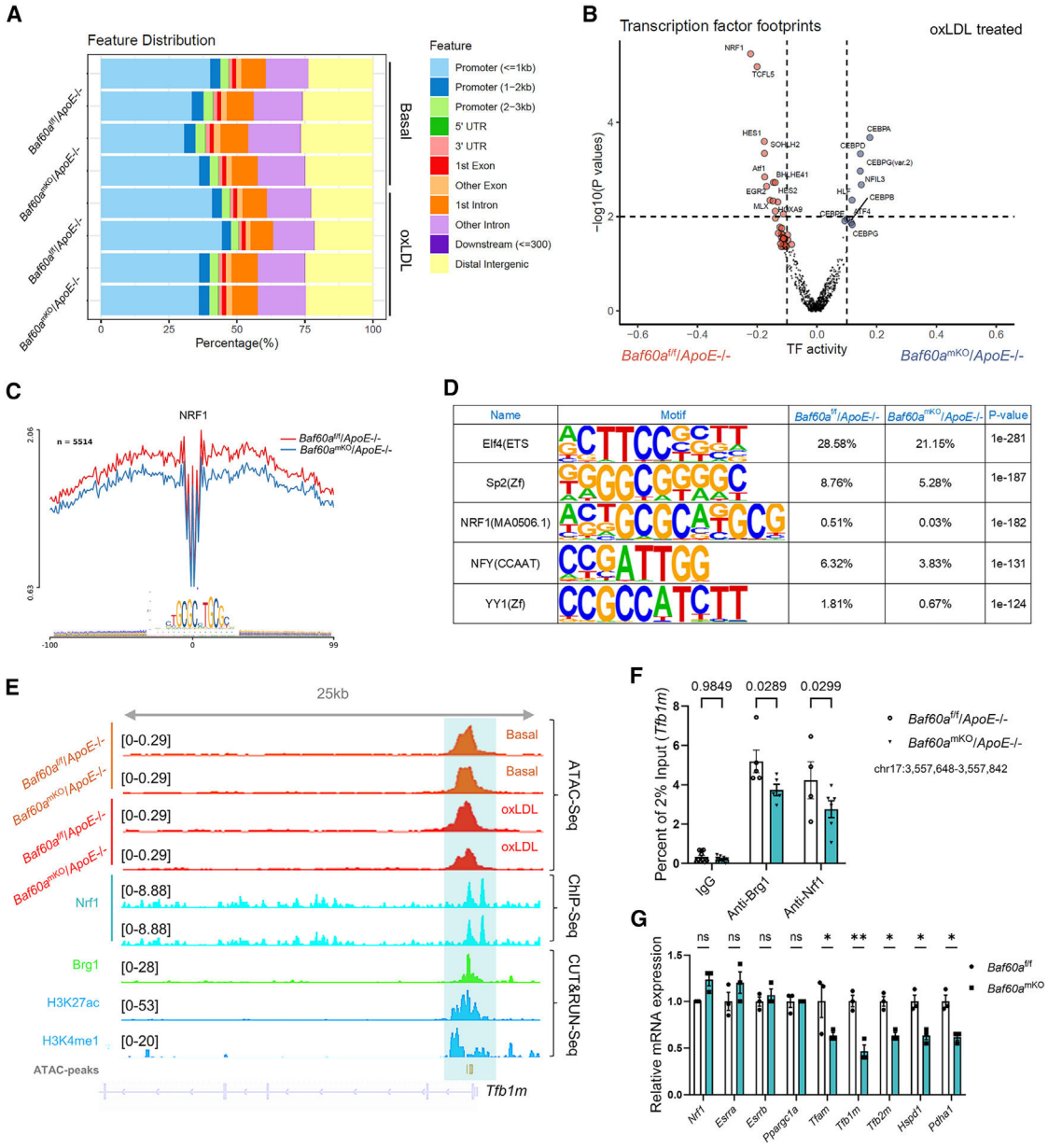

Figure 6. BAF60a deficiency impairs NRF1 transcriptional response to atherosclerotic stress and reduces NRF1 targeted gene expression

BMDMs from *Baf60a*^{mKO}/*ApoE*$^{-/-}$ or *Baf60a*$^{f/f}$/*ApoE*$^{-/-}$ mice were treated with either vehicle control or oxLDL (50 μg/mL, 48 h).

(A) Peak feature distribution across different chromatin regions.

(B–D) ATAC-seq followed by transcription factor (TF) footprint and motif analysis (n = 2 for each condition). (B) Volcano plot of TF footprints with top differential activities. (C) NRF1 footprint within 100 bp of the seed region. (D) HOMER motif enrichment analysis of top five differentially enriched motifs based on p value.

(E) Genome track view of chromatin accessibility around selected NRF1-targeted *Tfb1m* gene loci by *Baf60a*^{mKO}/*ApoE*$^{-/-}$ or *Baf60a*$^{f/f}$/*ApoE*$^{-/-}$ BMDMs ATAC-seq, Nrf1 ChIP-

seq (GEO: GSE208936), and CUT&RUN-seq for Brg1, H3K27ac, and H3K4me1 (GEO: GSE192777).

(F) ChIP assay of BRG1 and NRF1 binding on the peak region of *Tfb1m* promoter determined above.

(G) qPCR quantification of potential BAF60a-interacting TF/co-factors and NRF1-regulated mitochondria genes (n = 3).

Data are presented as mean ± SEM. Two-way ANOVA followed by Holm-Sidak post hoc analysis for (F) and (G). ns, none significant; *p < 0.05; **p < 0.01.

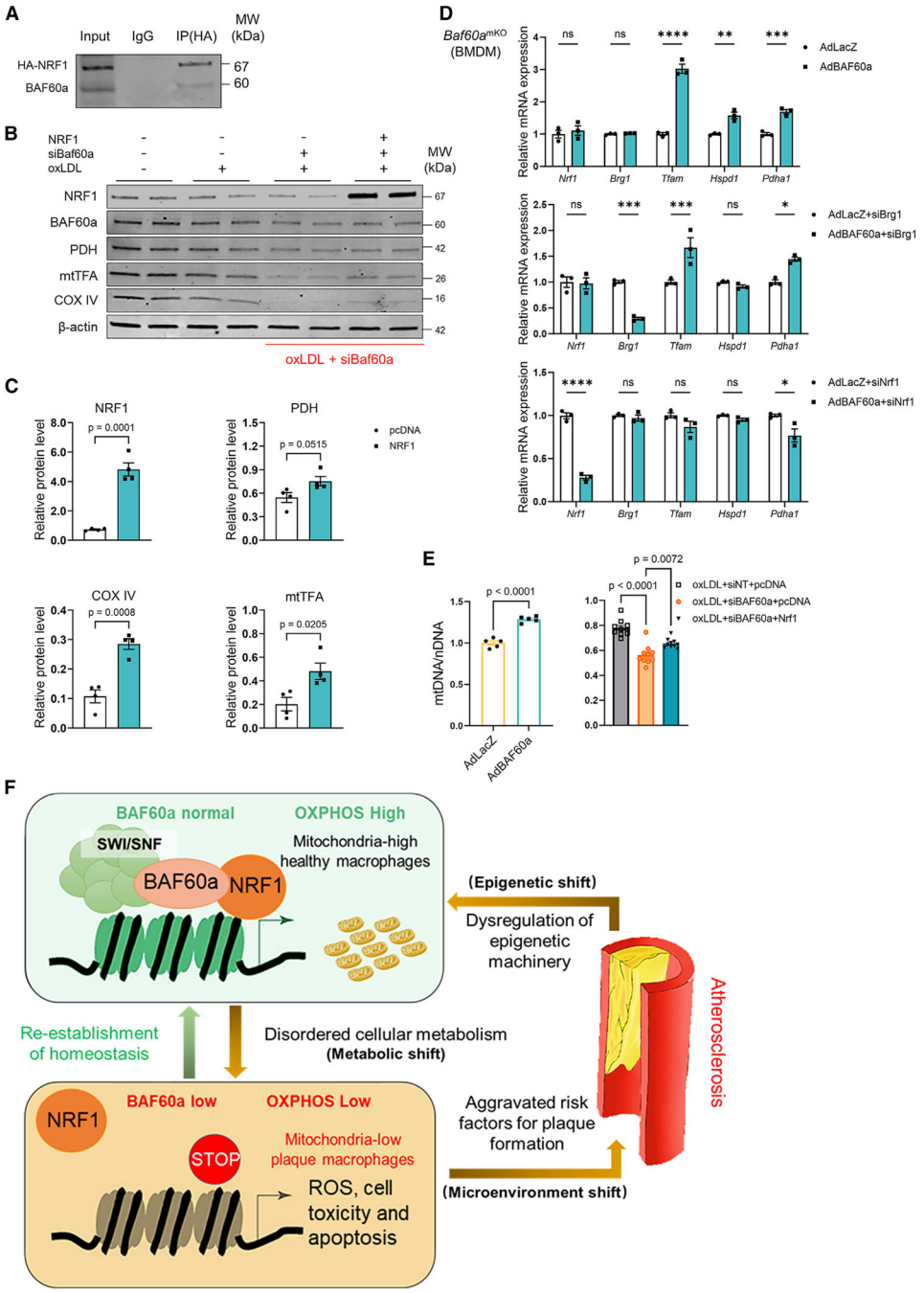

Figure 7. BAF60a interacts with NRF1, and its overexpression requires NRF1 to alleviate mitochondrial dysfunction

(A) Co-IP of the physical interaction between NRF1 and BAF60a in RAW264.1 cells overexpressing HA-NRF1, with immunoglobulin G (IgG) as a negative control.

(B) Immunoblotting of RAW264.7 cells co-transfected with siNT/siBaf60a and pcDNA/*NRF1* for 48 h followed by treatment of either control or oxLDL (50 μg/mL, 24 h).

(C) Quantification of mitochondrial-related protein changes in response to *NRF1* overexpression in (B) (n = 4).

(D) BMDMs from *Baf60a*^{mKO} mice were infected with either AdLacZ or AdBAF60a and transfected with vehicle, siBrg1, or siNrf1 for 48 h before treatment with oxLDL (50 μg/mL, 48 h). qPCR was performed to quantify Nrf1-regulated gene expression (n = 3).
(E) mtDNA-to-nDNA ratio quantified by qPCR. Left: BMDMs from *Baf60a*^{mKO} mice were infected with either AdLacZ or AdBAF60a for 24 h and treated with oxLDL (50 μg/mL, 48 h, n = 5). Right: RAW264.7 cells were co-transfected with siNT/siBaf60a and pcDNA/*Nrf1* for 48 h and treated by either control or oxLDL (50 μg/mL, 24 h, n = 10).
(F) Schematic model of BAF60a regulation of plaque macrophage and mitochondria homeostasis in atherosclerosis.
Data are presented as mean ± SEM. Student's t test for (C) and (E) (left); ordinary one-way ANOVA by Tukey's post hoc analysis for (E) (right); two-way ANOVA followed by Holm-Sidak post hoc analysis for (D). ns, none significant; *p < 0.05; **p < 0.01; ***p < 0.001; ****p < 0.0001.

KEY RESOURCES TABLE

REAGENT or RESOURCE	SOURCE	IDENTIFIER
Antibodies		
Rabbit anti-BAF60a antibody	Abcam	Cat#ab245222; RRID:AB_3065059
Rabbit anti-BAF60b antibody	Abcam	Cat#ab220164; RRID:AB_2904257
Rabbit anti-BRG1 antibody	Abcam	Cat#ab110641; RRID:AB_10861578
Rabbit anti-BAF155 antibody	Cell Signaling Technology	Cat#11956; RRID:AB_2797776
Rabbit anti-BRD9 antibody	Cell Signaling Technology	Cat#71232; RRID:AB_2799798
Rabbit anti-PDH antibody	Cell Signaling Technology	Cat#3205; RRID:AB_2162926
Mouse anti-β-actin antibody	Cell Signaling Technology	Cat#3700; RRID:AB_2242334
Rabbit anti-DYKDDDDK antibody	Cell Signaling Technology	Cat#14793S; RRID:AB_2572291
Rabbit anti-HA antibody	Cell Signaling Technology	Cat#3724; RRID:AB_1549585
Rabbit anti-TFAM antibody	Thermo Fisher Scientific	Cat#PA5–68789; RRID:AB_2688635
Rabbit anti-NRF1 antibody	Thermo Fisher Scientific	Cat#PA5–27854; RRID:AB_2545330
Rabbit anti-Apolipoprotein B antibody	Thermo Fisher Scientific	Cat#MA5–35458; RRID:AB_2849359
Rat anti-Galectin 3 (Mac2) antibody	Thermo Fisher Scientific	Cat#14–5301-82; RRID:AB_837132
Rat anti-CD16/CD32 (Fc blocker) antibody	Thermo Fisher Scientific	Cat#14–0161-85; RRID:AB_467134
EF450 Rat anti-CD45 Monoclonal antibody	Thermo Fisher Scientific	Cat#48–0451-82; RRID:AB_1518806
EF660 Rat anti-Galectin 3 antibody	Thermo Fisher Scientific	Cat#50–5301-82; RRID:AB_11220276
PerCP-Cy5.5 Rat anti-CD3 antibody	Thermo Fisher Scientific	Cat#45–0031-82; RRID:AB_1107000
Mouse anti-BAF60a antibody	BD Biosciences	Cat#611728; RRID:AB_2192143
FITC Rat anti-mouse CD19 antibody	BD Biosciences	Cat#557398; RRID:AB_396681
Rabbit anti-COX4 antibody	Novus Biologicals	Cat#NB110–39115; RRID:AB_789419
680RD Donkey anti-rabbit IRDye	LI-COR Biosciences	Cat#926–68073; RRID:AB_10954442
800CW Donkey anti-rabbit IRDye	LI-COR Biosciences	Cat#926–32213; RRID:AB_621848
680RD Donkey anti-mouse IRDye	LI-COR Biosciences	Cat#926–68072; RRID:AB_10953628
800CW Donkey anti-mouse IRDye	LI-COR Biosciences	Cat#926–32212; RRID:AB_621847
Alexa Fluor 594 donkey anti-rat antibody	Jackson ImmunoResearch	Cat#712–585-153; RRID:AB_2340689
FITC Rat anti-mouse Ly-6G antibody	BioLegend	Cat#127605; RRID:AB_1236488
APC Rat anti-CD11b antibody	BioLegend	Cat#101225; RRID:AB_830641
APC F4/80 Rat anti-mouse antibody	Cytek Biosciences/Tonbo	Cat#20–4801; RRID:AB_2621602
Mouse anti-HA antibody	ABclonal	Cat#AE008; RRID:AB_2770404
anti-F4/80 MicroBeads	Miltenyi Biotec	Cat#130–110-443; RRID:AB_2858241
anti-CD11b MicroBeads	Miltenyi Biotec	Cat#130–049-601; RRID:AB_2927377
Bacterial and virus strains		
Ad-Flag-hBAF60a	Lab prep	N/A
Ad-LacZ	Lab prep	N/A
Biological samples		
Low-Density Lipoprotein (LDL)	Lee Biosolutions	Cat#360–10

REAGENT or RESOURCE	SOURCE	IDENTIFIER
Oxidized LDL	Lap prep	N/A
Chemicals, peptides, and recombinant proteins		
Recombinant human TNFα	R&D Systems	Cat#210-TA
7-Keto cholesterol	Cayman Chemical	Cat#16339
Calcein AM	Cayman Chemical	Cat#14948
Recombinant Mouse M-CSF	Thermo Fisher Scientific	Cat#416-ML
Collagenases I	Thermo Fisher Scientific	Cat#17100–017
NucBlue™	Thermo Fisher Scientific	Cat#R37605
Phenol:Chloroform: Isoamyl Alcohol (25:24:1,v/v)	Thermo Fisher Scientific	Cat#15593049
MitoTracker™ Deep Red FM	Thermo Fisher Scientific	Cat#M22426
MitoSOX™ Red	Thermo Fisher Scientific	Cat#M36008
HCS LipidTOX™ Green	Thermo Fisher Scientific	Cat#H34475
TMRM	Thermo Fisher Scientific	Cat#T668
Hoechst	Thermo Fisher Scientific	Cat#H3570
TRIzol	Thermo Fisher Scientific	Cat#15596018
ProLong™ Gold Antifade Mountant with DAPI	Thermo Fisher Scientific	Cat#P36935
Lipofectamine 2000	Thermo Fisher Scientific	Cat#1668019
Lipofectamine RNAi Max	Thermo Fisher Scientific	Cat#13778150
Protease inhibitor cocktail	Thermo Fisher Scientific	Cat#11873580001
PhosSTOP phosphatase inhibitors	Thermo Fisher Scientific	Cat#4906845001
RIPA buffer	Thermo Fisher Scientific	Cat#89901
Non Fat Dry Milk	Thermo Fisher Scientific	Cat#NC9121673
USDA HI FBS	Thermo Fisher Scientific	Cat#10438026
MEM NEAA	Thermo Fisher Scientific	Cat#11140050
Sodium pyruvate	Thermo Fisher Scientific	Cat#11360070
eFluor 450 isotype control (rat IgG2b kappa)	Thermo Fisher Scientific	Cat#48–4031-82
APC conjugated isotype control (rat IgG2a kappa)	Thermo Fisher Scientific	Cat#17–4321-81
PerCP-cy5.5 isotype control (eBR2a)	Thermo Fisher Scientific	Cat#45–4321-80
eFlour 660 isotype control (rat IgG2a Kappa)	Thermo Fisher Scientific	Cat#50–4321-82
4% Paraformaldehyde in PBS	Thermo Fisher Scientific	Cat#AAJ19943K2
10% Buffered Formalin	Thermo Fisher Scientific	Cat#23–245685
TRYPSIN 0.25% EDTA	Thermo Fisher Scientific	Cat#25200–056
Collagenase from *Clostridium histolyticum*	Sigma-Aldrich	Cat#C7657
Hyaluronidase	Sigma-Aldrich	Cat#H3606
DNase-I	Sigma-Aldrich	Cat#10104159001
Lipopolysaccharides from Escherichia coli O111:B4	Sigma-Aldrich	Cat#L2630
Ficoll-Paque PREMIUM 1.084	Sigma-Aldrich	Cat#GE17–5446-02
Bovine Serum Albumin	Sigma-Aldrich	Cat#A8806
Donkey Serum	Sigma-Aldrich	Cat#S30–100ML
Oil red O	Sigma-Aldrich	Cat#O0625

REAGENT or RESOURCE	SOURCE	IDENTIFIER
Phosphate Buffered Saline	Sigma-Aldrich	Cat#P3813
Protein G Magnetic Beads	Cell Signaling Technology	Cat#70024
Cell Lysis Buffer	Cell Signaling Technology	Cat#9803
PMSF	Cell Signaling Technology	Cat#8553
Rabbit IgG	Cell Signaling Technology	Cat#2729
RNase-free DNase I	QIAGEN	Cat#79254
O.C.T. Compound	Tissue-Tek	Cat#4583
SYBR Green Fast qPCR Mix	Abclonal	Cat#RK21203
Nucleic Acid Transfection Enhancer	InvivoGen	Cat#lyec-nate
FITC isotype control	Biolegend	Cat#400110
APC-Cy7 isotype control	Biolegend	Cat#400623
Heparin	UMHS pharmacy	Cat#6543
Tris/Glycine/SDS	Bio-Rad	Cat#1610772
Tris/Glycine	Bio-Rad	Cat#1610771
10% Tween 20	Bio-Rad	Cat#1610781
Accutase	Stemcell technologies	Cat#07920
Critical commercial assays		
EdU Assay	Abcam	Cat#ab222421
Cholesterol fluorometric test kit	Cayman Chemical	Cat#10007640
Colorimetric-based Cholesterol E assay	Fujifilm Wako Diagnostics	Cat#999–02601
Colorimetric-based Triglyceride assay	Fujifilm Wako Diagnostics	Cat#290–63701
Glucose test strips	Ascensia	Cat#0193–7308-50
RNeasy Mini Kit	Qiagen	Cat#74106
SuperScript III kit	Thermo Fisher Scientific	Cat#18080051
Human Monocyte Nucleofector™ Kit	Lonza Biosciences	Cat#VPA-1007
Seahorse XFp Cell Mito Stress Test Kit	Agilent Technologies	Cat#103010–100
FITC Annexin V Apoptosis Detection Kit I	BD Biosciences	Cat#556547
ApopTag Peroxidase *In Situ* Apoptosis Detection Kit	Sigma-Aldrich	Cat#S7100
LDH assay kit	Sigma-Aldrich	Cat#MAK066
SimpleChIP Enzymatic Chromatin IP Kit (Magnetic Beads)	Cell Signaling Technology	Cat#9003S
Deposited data		
RNA-seq (original)	Gene Expression Omnibus	GSE224664, GSE224665
ChIP-seq (original)	Gene Expression Omnibus	GSE224666
ATAC-seq (original)	Gene Expression Omnibus	GSE224667
Raw data (original)	Mendeley Data	https://doi.org/10.17632/2v6vfjw8j4.1
Experimental models: Cell lines		

REAGENT or RESOURCE	SOURCE	IDENTIFIER
AD-293	Agilent Technologies	Cat#240085
THP-1	ATCC	Cat#TIB-202
RAW 264.7	ATCC	Cat#TIB-71
Human Aortic Endothelial Cell (HAEC)	Lonza Biosciences	Cat#CC-2535
Mouse bone marrow-derived macrophages	Lab prep	N/A
Mouse peripheral blood mononuclear cell (PMBC)	Lab prep	N/A
Experimental models: Organisms/strains		
Mouse: B6: C57BL/6J	The Jackson Laboratory	JAX: 000664
Mouse: ApoE$^{-/-}$: B6.129P2-*Apoe*^{tm1Unc}/J	The Jackson Laboratory	JAX: 002052
Mouse: Lyz2^{+}: B6.129P2-Lyz2$^{tm1(cre)Ifo/J}$	The Jackson Laboratory	JAX: 004781
Mouse: *Baf60a*$^{f/f}$: B6.Cg-*Smarcd1*$^{tm1.1Jddl}$/J	Lab bred/The Jackson Laboratory	JAX: 036171
Mouse: *Baf60a*^{mKO}: *Baf60a*$^{f/f}$/Lyz2+	Lab bred	N/A
Mouse: *Baf60a*^{mKO}/ApoE$^{-/-}$	Lab bred	N/A
Mouse: *Baf60a*$^{f/f}$/ApoE$^{-/-}$	Lab bred	N/A
Oligonucleotides		
siSmarcd1	Dharmacon	Cat#L-046893–01-0005
siSMARCD1	Dharmacon	Cat#L-017244–00-0005
siNrf1	Dharmacon	Cat#J-041037–09-0002
siSMARCA4	Dharmacon	Cat#J-041135–05-0002
siControl pool2	Dharmacon	Cat#D-001206–14-05
qPCR primers	Table S1	N/A
Recombinant DNA		
pCMV3-N-HA-NRF1	SinoBiological	MG52011-NY
pcDNA3.1+	Lab maintained	N/A
pcDNA3.1-N-Flag-BAF60a	Lab prep	N/A
pcDNA3.1-N-Flag-BAF60a$_{(D1–114)}$	Lab prep	N/A
pcDNA3.1-N-Flag-BAF60a$_{(D1–176)}$	Lab prep	N/A
pcDNA3.1-N-Flag-BAF60a$_{(D115–515)}$	Lab prep	N/A
pcDNA3.1-N-Flag-BAF60a$_{(D130–515)}$	Lab prep	N/A
pcDNA3.1-N-Flag-BAF60a$_{(D177–515)}$	Lab prep	N/A
pcDNA3.1-N-Flag-BAF60a$_{(D307–515)}$	Lab prep	N/A
pcDNA3.1-N-Flag-BAF60a$_{(D177–306)}$	Lab prep	N/A
pcDNA3.1-N-Flag-BAF60a$_{(D407–422)}$	Lab prep	N/A
Software and algorithms		
Prism	GraphPad Software	https://www.graphpad.com/features
Fiji: ImageJ	NIH/LOCI	https://github.com/fiji/fiji

REAGENT or RESOURCE	SOURCE	IDENTIFIER
Empiria Studio	LI-COR	https://www.licor.com/bio/empiria-studio
FlowJo	BD Biosciences	https://www.flowjo.com/
Seahorse Wave Desktop	Agilent	https://www.agilent.com/en/product/cell-analysis/real-time-cell-metabolic-analysis/xf-software/seahorse-wave-desktop-software-740897
FastQC	Babraham Institute	https://www.bioinformatics.babraham.ac.uk/projects/fastqc/
TrimGalore	Babraham Institute	https://www.bioinformatics.babraham.ac.uk/projects/trim_galore/
Cutadapt	NBIS (National Bioinformatics Infrastructure Sweden)	https://github.com/marcelm/cutadapt
Bowtie2	Langmead and Salzberg et al.[88]	https://github.com/BenLangmead/bowtie2
Picard	Broad Institute	https://github.com/broadinstitute/picard
Samtools	Li et al.[89]	https://www.htslib.org/
Bedtools	Quinlan and Hall et al.[90]	https://bedtools.readthedocs.io/en/latest/
Macs2	Zhang et al.[91]	https://pypi.org/project/MACS2/
DeepTools	Max Planck Institute for Immunobiology and Epigenetics	https://github.com/deeptools/deepTools
MultiQC	Ewels et al.[92]	https://multiqc.info/
Ataqv	The Parker Lab	https://github.com/ParkerLab/ataqv
ChIPseeker	Yu, Wang, and He et al.[93]	https://guangchuangyu.github.io/software/ChIPseeker/
HOMER	University of California San Diego	http://homer.ucsd.edu/homer/motif/
HINT-ATAC	Regulatory Genomics Toolbox	https://github.com/CostaLab/reg-gen
DESeq2	Love et al.[94]	https://bioconductor.org/packages/release/bioc/html/DESeq2.html
GSEA	University of California San Diego/Broad Institute	https://www.gsea-msigdb.org/gsea/index.jsp
Seurat	Satija lab	https://satijalab.org/seurat/
CIBERSORTx	Alizadeh Lab and Newman Lab	https://cibersortx.stanford.edu/
ClusterProfiler	Yu et al.[95]	https://guangchuangyu.github.io/software/clusterProfiler/
Other		
Western diet (WD)	Envigo	Cat#TD.88137
Iscove's Modified Dulbecco's Media	GIBCO	Cat#12440053
Dulbecco's Modified Eagle Medium	GIBCO	Cat#11965092
Roswell Park Memorial Institute (RPMI) 1640 Medium	GIBCO	Cat#11875093
Dulbecco's phosphate-buffered saline (DPBS)	GIBCO	Cat# 14190250

REAGENT or RESOURCE	SOURCE	IDENTIFIER
EGM™-2 Endothelial Cell Growth Medium-2 BulletKit™	Lonza	Cat# CC-3162